



Interseismic Coupling and Slow Slip Events on the Cascadia Megathrust

SYLVAIN MICHEL,^{1,2}  ADRIANO GUALANDI,^{2,3} and JEAN-PHILIPPE AVOUAC²

Abstract—In this study, we model geodetic strain accumulation along the Cascadia subduction zone between 2007.0 and 2017.632 using position time series from 352 continuous GPS stations. First, we use the secular linear motion to determine interseismic locking along the megathrust. We determine two end member models, assuming that the megathrust is either a priori locked or creeping, which differ essentially along the trench where the inversion is poorly constrained by the data. In either case, significant locking of the megathrust updip of the coastline is needed. The downdip limit of the locked portion lies $\sim 20\text{--}80$ km updip from the coast assuming a locked a priori, but very close to the coast for a creeping a priori. Second, we use a variational Bayesian Independent Component Analysis (vbICA) decomposition to model geodetic strain time variations, an approach which is effective to separate the geodetic strain signal due to non-tectonic and tectonic sources. The Slow Slip Events (SSEs) kinematics is retrieved by linearly inverting for slip on the megathrust the Independent Components related to these transient phenomena. The procedure allows the detection and modelling of 64 SSEs which spatially and temporally match with the tremors activity. SEEs and tremors occur well inland from the coastline and follow closely the estimated location of the mantle wedge corner. The transition zone, between the locked portion of the megathrust and the zone of tremors, is creeping rather steadily at the long-term slip rate and probably buffers the effect of SSEs on the megathrust seismogenic portion.

Key words: Cascadia megathrust, slow slip events, interseismic coupling, variational bayesian independent component analysis.

1. Introduction

The Juan de Fuca (JdF) plate subducts beneath the North American plate along the Cascadia megathrust off the coast of southwestern Canada and northwestern United States (Fig. 1). This subduction system is a typical warm case example, due to the subducting plates young age (< 10 Ma) and moderate convergence rates ($27\text{--}45$ mm/year) (e.g. Hyndman et al. 1997; DeMets and Dixon 1999).

The Cascadia megathrust hosted an $M \sim 9$ earthquake in 1700, producing a tsunami that was reported in Japan (Satake et al. 2003). Additional $M \sim 9$ in the last 10 000 years have been documented from turbidite sequences (Goldfinger et al. 2017), tsunami deposits and coastal geological evidence (Atwater 1987; Clague and Bobrowsky 1994; Atwater and Hemphill-Haley 1997; Kelsey et al. 2005; Wang et al. 2013; Kemp et al. 2018). However, since 1700, the megathrust has remained relatively silent. At present, the background seismicity is very quiet except at its Northern and Southern ends (Wang and Trehu 2016).

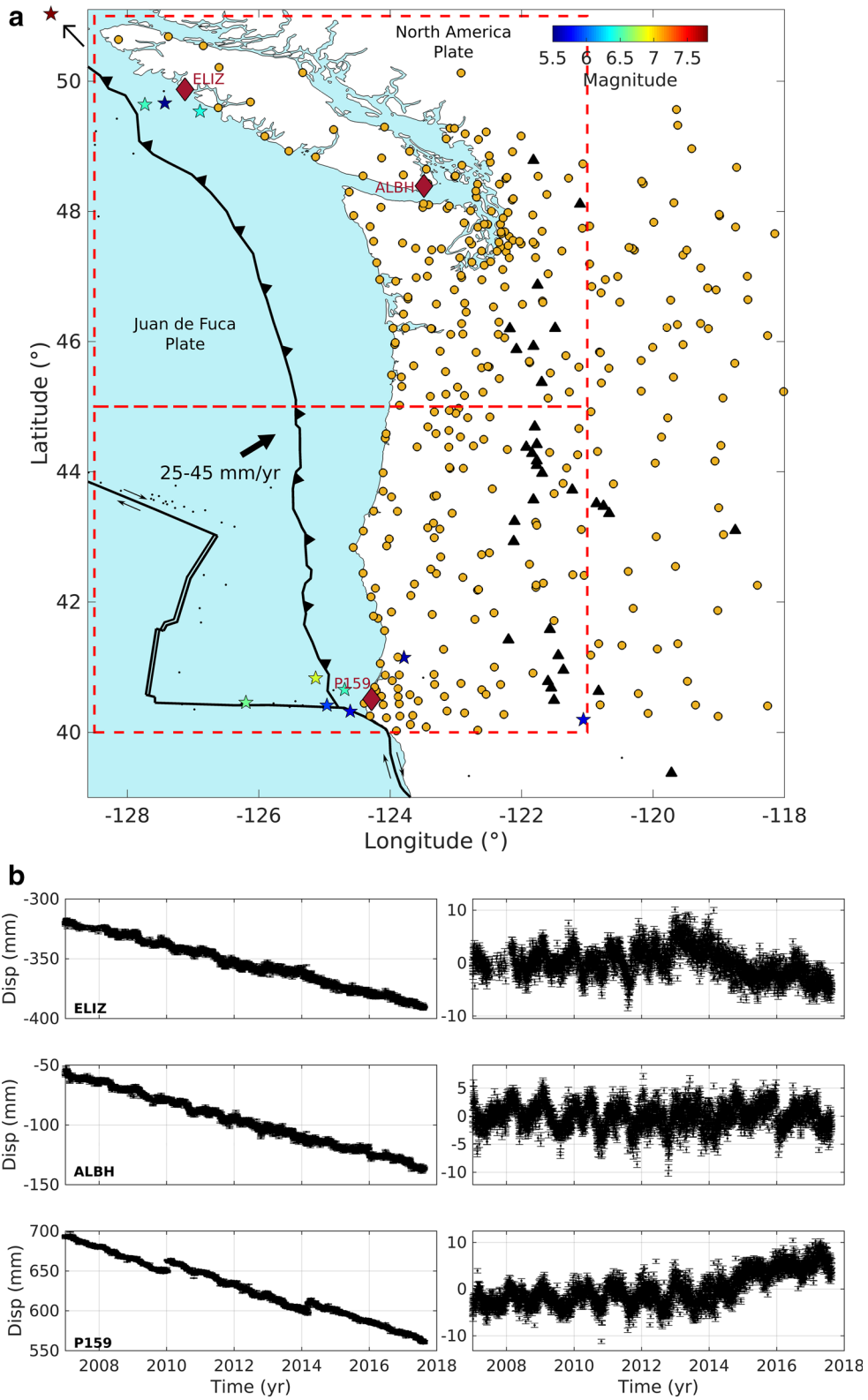
The interseismic loading retrieved from surface geodetic measurements allowed to estimate the degree of locking of the megathrust and create maps of interseismic coupling (defined as the ratio of slip deficit rate along the megathrust, determined from the geodetic interseismic data, and the long-term slip rate). Interseismic coupling maps are useful for seismic hazard assessment as locked portions of the megathrust are indeed expected to potentially slip in large interplate earthquakes as has been observed in several seismically active regions (e.g. Chlieh et al. 2008; Moreno et al. 2010; Loveless and Meade 2011). Previous inversions of geodetic strain rate measured onshore indicate that the megathrust is locked to some degree in the interseismic period

Electronic supplementary material The online version of this article (<https://doi.org/10.1007/s00024-018-1991-x>) contains supplementary material, which is available to authorized users.

¹ Bullard Laboratories, Department of Earth Sciences, University of Cambridge, Madingley Road, Cambridge, Cambridgeshire CB3 0EZ, UK. E-mail: sylvain_michel@live.fr

² Department of Geology and Planetary Sciences, California Institute of Technology, 1200 E California Blvd, Pasadena, CA 91125, USA. E-mail: adriano.geolandi@gmail.com; avouac@gps.caltech.edu

³ Jet Propulsion Laboratory, California Institute of Technology, 4800 Oak Grove Dr, Pasadena, CA 91109, USA.



◀Figure 1

a Distribution of GPS stations (yellow dots) along the Cascadia subduction zone. The black lines are the plate boundaries and the black triangles indicate active volcanoes locations (USGS). The black dots indicate M5.5 + seismicity from 1984 to 2017 (ANSS catalogue). The stars indicate the 11 earthquakes that affected the GPS stations, the colour indicating their magnitude. The red diamonds indicate, from North to South, the location of the stations ELIZ, ALBH and P159. The two dashed red rectangles delimit the North and South sections as indicated in Sect. 3.1.2. **b** Left panels indicate the East component raw time series for the stations ELIZ, ALBH and P159. The right panels show the detrended, time series of those 3 stations corrected for offsets and regional tectonics using the block model of Schmalz et al. (2014)

(Hyndman et al. 1997; Wang et al. 2003). We use the secular velocity field from 352 continuous GPS (cGPS) stations corrected for post-glacial rebound using the model of Peltier et al. (2015), to determine an interseismic coupling map for the 2007–2017 period. We also determine temporal variations of slip along the megathrust over that time period to clarify the relative position of the portions of the megathrust that are locked in the interseismic period and those that are producing transient slip events. The geodetic position time series from Cascadia show strong temporal variations which indicate episodic aseismic slip events, commonly called Slow Slip Events (SSEs) (Dragert et al. 2001; Miller et al. 2002). These slip events are mostly aseismic but are correlated in time and space with tremors (Rogers and Dragert 2003; Wech and Bartlow 2014), which presumably occur on the plate interface (Wech and Creager

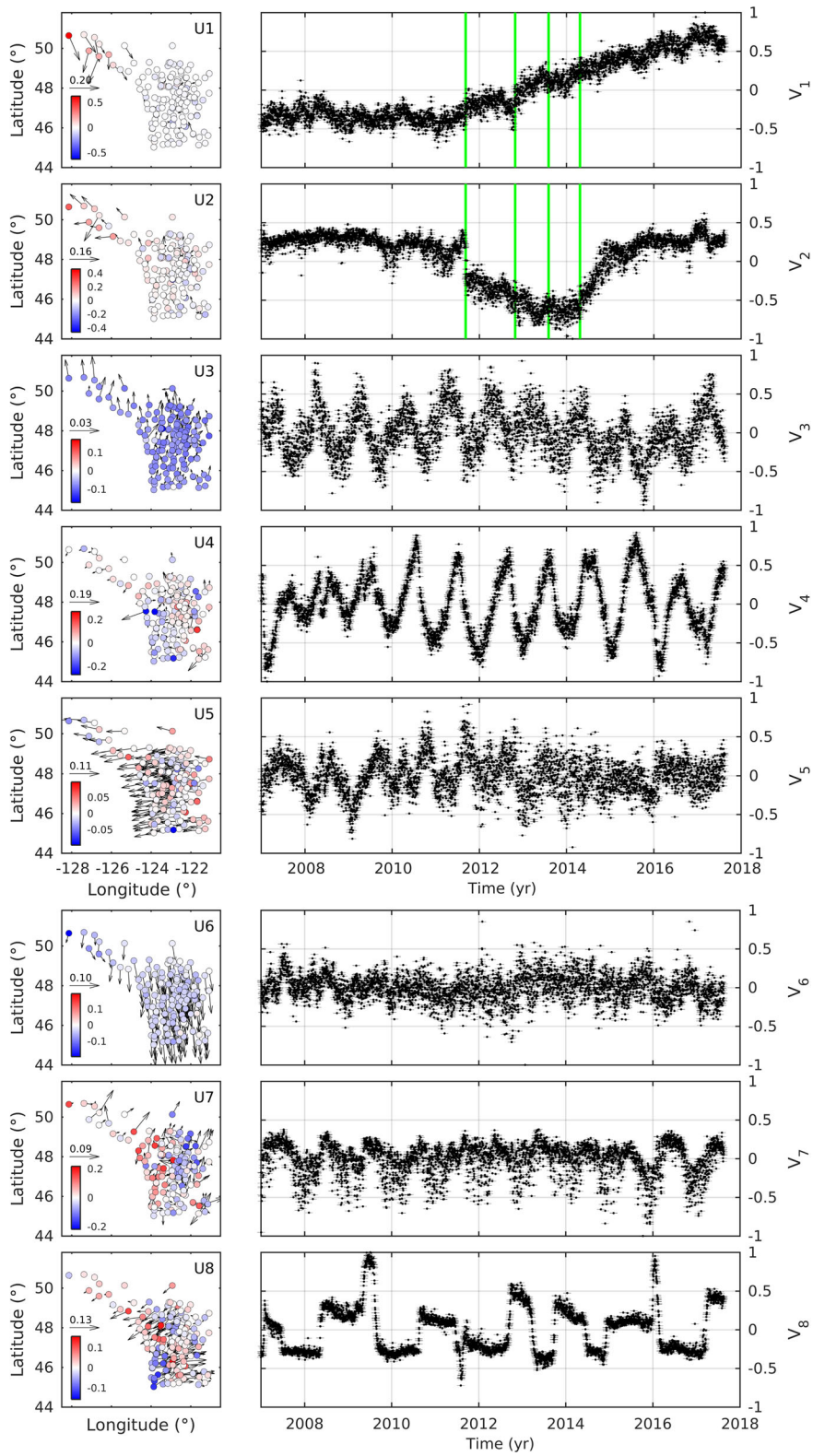
2007). It is, therefore, likely that SSEs are related to episodic slip along the megathrust. SSEs are, however, not the only source of variation of the geodetic time series from their secular trend. These variations can be related to various causes. The larger earthquakes in the area may have caused some offsets and transient post-seismic deformation. The geodetic time series also show variations that are seasonal and likely due to surface load variations as has been observed in various other settings (Blewitt et al. 2001; Bettinelli et al. 2008; Fu et al. 2012). Temporal variations in geodetic series can also be spurious due to the ITRF realization generally used to express position in a global reference frame (Dong et al. 2002).

In this study, we analyse the geodetic position time series from Cascadia with the objective of separating the terms due to the various temporally varying factors and to interseismic coupling. To that effect, we apply to the detrended position time series a variational Bayesian Independent Component Analysis (vbICA) (Choudrey and Roberts 2003), a signal processing technique which has proven to be effective in extracting different sources of deformation (afterslip, SSEs, and seasonal signals) in geodetic time series (Gualandi et al. 2016, 2017a, b, c). We next perform an inversion of the Independent Components (ICs) related to SSEs, following the general approach of the principal component analysis-based inversion method (Kositsky and Avouac 2010). With this vbICA-based Inversion Method, (vbICA-IM), we

Table 1

Earthquakes affecting GPS time series from the North and South section (USGS)

Section	Magnitude	Year	Month	Day	Latitude	Longitude	Depth
North	6.4	2011	9	9	49.535	126.893	22
	7.8	2012	10	28	52.788	132.101	14
	5.5	2013	8	4	49.661	127.429	10
	6.5	2014	4	24	49.639	127.732	10
South	6.5	2010	1	10	40.652	124.693	28.7
	5.9	2010	2	4	40.412	124.961	23
	5.6	2012	2	13	41.143	123.79	27.4
	5.7	2013	5	24	40.192	121.06	8
	6.8	2014	3	10	40.829	125.134	16.4
	5.7	2015	1	28	40.318	124.607	16.9
	6.6	2016	12	8	40.454	126.194	8.5



◀Figure 2

Spatial and temporal functions of the independent components obtained from applying a vbICA decomposition to the data from the Northern area (see location in Fig. 1) for 8 components. The left panels show the spatial functions (matrix U). The arrows and the coloured dots indicate horizontal and vertical motion, respectively. The right shows the temporal functions (matrix V). The green lines indicate the timing of the earthquakes of the northern section as indicated in Table 1. We consider components 1 and 2 to be related to post-seismic displacements following earthquakes in the North (Fig. 1 and Table 1)

produce a kinematic model of the spatio-temporal variation of slip on the Megathrust from 2007 to 2017. We also determine the pattern of interseismic coupling along the megathrust from inverting the secular geodetic signal due to interseismic strain.

The remaining of the manuscript is organized as follows. We first introduce the data considered in this study in Sect. 2. We then describe how we extract the signals related to the different sources of interest. In Sects. 4 and 5, we present the results of the inversion to retrieve interseismic coupling and the SSEs kinematics, respectively. Final remarks and further discussions conclude the manuscript.

2. Data

We use daily sampled position time series in the IGS08 reference frame from the Pacific Geodetic Array (PANGA) and the Plate Boundary Observatory (PBO) maintained by UNAVCO and processed by the Nevada Geodetic Laboratory (<http://geodesy.unr.edu>, last access August 2017). Most of the available continuous GPS (cGPS) stations were deployed in 2007, and we consider the time range that goes from 2007.0 to 2017.632. We use only time series with at most 40% of missing data and we exclude all the stations in the proximity (< 15 km) of volcanoes to avoid contamination by volcanic signals. We also discard station BLYN because of spurious large displacements of unknown origin that were clearly not observed at nearby stations. The final selection includes $N_{\text{GPS}} = 352$ cGPS stations (Fig. 1a). We then refer all the stations to the North America reference frame using the regional block model of Schmalzer et al. (2014). The position time series are then organized in a $M \times T$ matrix X_{obs} , where

$M = 3 \times N_{\text{GPS}}$ is the total number of time series (East, North, and Vertical direction per each station), and $T = 3883$ is the total number of observed epochs.

Two tremor catalogues are used in this study, one from Ide (2012) between 2007 and 2009.595, and one from the Pacific Northwest Seismic Network (PNSN) catalogue from 2009.595 to 2017.632 (<https://pnsn.org/tremor>).

3. Signal Extraction

Our goal is to retrieve: (1) the secular strain rate due to the average pattern of locking of Cascadia’s megathrust, and (2) the SSEs history on the megathrust in the considered time span.

To attain our first goal, we use the long-term linear trend estimated from a ‘trajectory’ model (Equation S1) in which each position time series is modelled using a combination of predetermined functions. We use a linear combination of a linear trend, annual and semi-annual terms, co-seismic step functions and exponential post-seismic functions. This approach provides a reasonable estimate of the linear trend with limited bias introduced by the non-linear terms. We do not model at this step the SSEs, but they do have a limited influence on the secular motion estimate since their typical returning period is much smaller than the overall observed time span, as it will be verified a posteriori. The secular geodetic velocities estimated from this approach are used to determine interseismic locking ratio on the Cascadia megathrust (Sect. 4). We use the long-term linear trend and the offsets that are simultaneously estimated by the trajectory model (Equation S1 and Supplementary Material) to correct the position time series. These time series are then the input for the variational Bayesian Independent Component Analysis (vbICA) algorithm. A brief description of the vbICA algorithm is offered in the next Sect. 3.1.1. We then describe its application to the extraction of post-seismic relaxation (Sect. 3.1.2), seasonal deformation (Sect. 3.1.3), and SSEs displacement (Sect. 3.1.4).

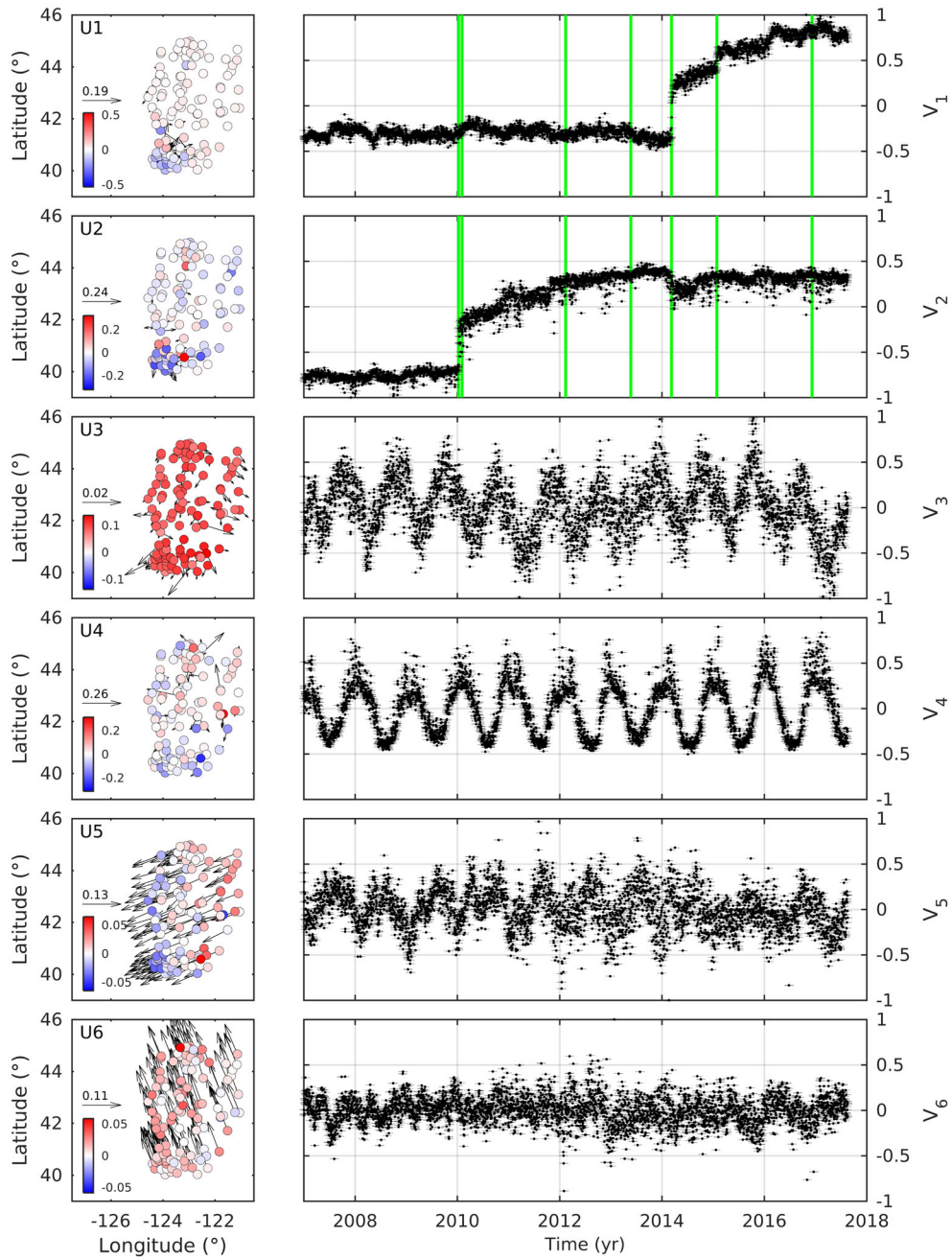


Figure 3

Spatial and temporal functions of the independent components obtained from applying a vbICA decomposition to the data from the Southern area (see location in Fig. 1) for 6 components. The left panels show the spatial functions (matrix U). The arrows and the coloured dots indicate horizontal and vertical motion, respectively. The right panels indicate the components temporal evolution (matrix V). The green lines indicate the timing of the earthquakes of the southern section as indicated in Table 1. We consider components 1 and 2 to be related to post-seismic displacements following earthquakes in the South (Fig. 1 and Table 1)

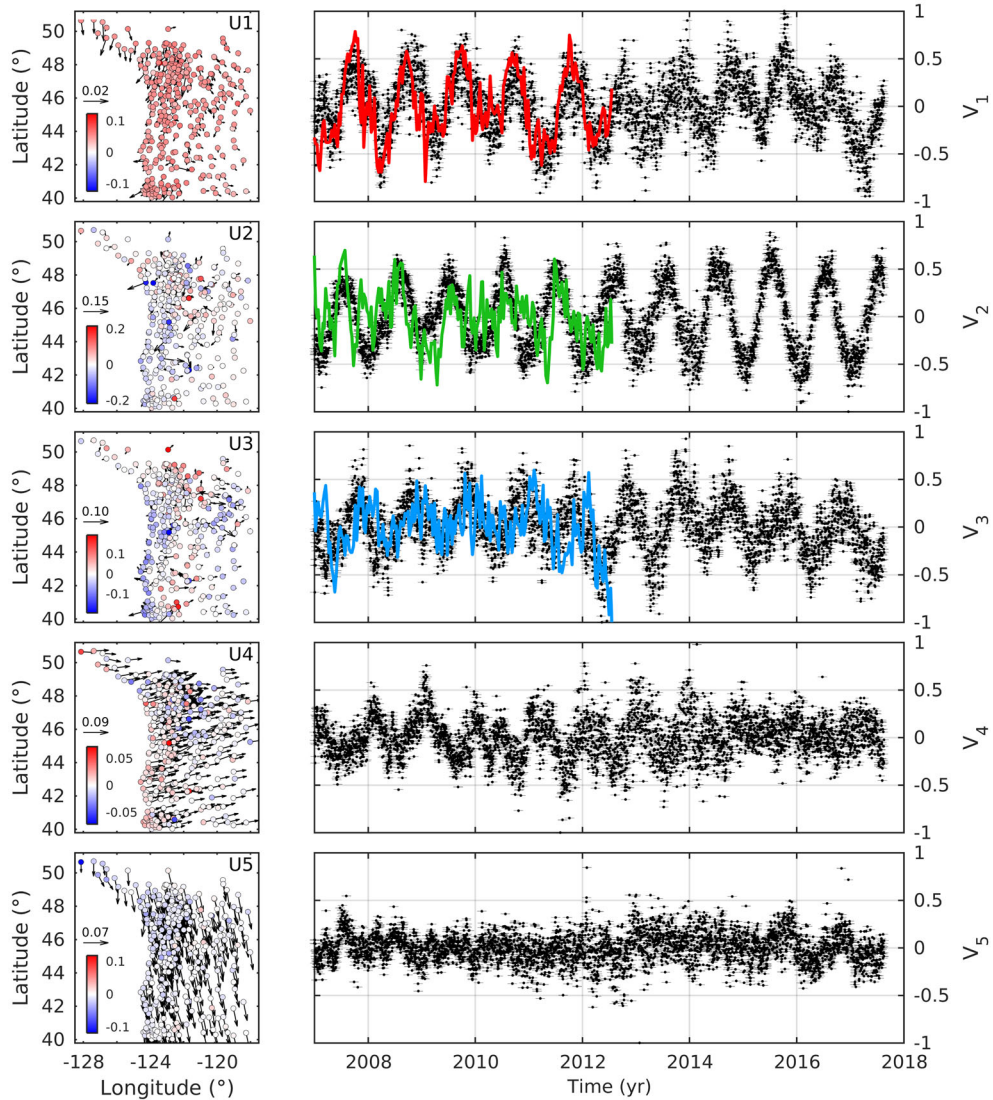


Figure 4

Spatial pattern and temporal evolution of each component of an 11-component decomposition (Sect. 3.1.3.). The left panels show the spatial pattern (matrix U). The arrows and the coloured dots indicate horizontal and vertical motions, respectively. The right panels show the components temporal functions (matrix V). The red, blue and green lines in the temporal evolution of components 1, 2 and 3 correspond to the temporal evolution of the components 1, 3 and 2, obtained from the decomposition of the theoretical geodetic time series due to surface load variations derived from GRACE. For clarity, they are plotted (right panels) separately and together with the temporal function of their associated components derived from the GPS time series (black dots). We consider components 1–3 to be seasonal deformation, 4 and 5 to be common mode, 6 to be a local effect, 7 to be seasonal scattered noise and 8–11 to be related to SSEs

3.1. Sse Surface Deformation Extraction

3.1.1 vbICA Algorithm

The vbICA algorithm allows the centered position time series (X) to be reconstructed by a linear combination of a limited number (R) of Independent

Components (ICs). The centring step is performed by removing from a time series its mean value. Each IC is fully characterized by a spatial distribution (U_r), a temporal function (V_r), and a relative weight (S_r). None of these quantities is a priori determined, allowing the data to reveal their inner structure. These

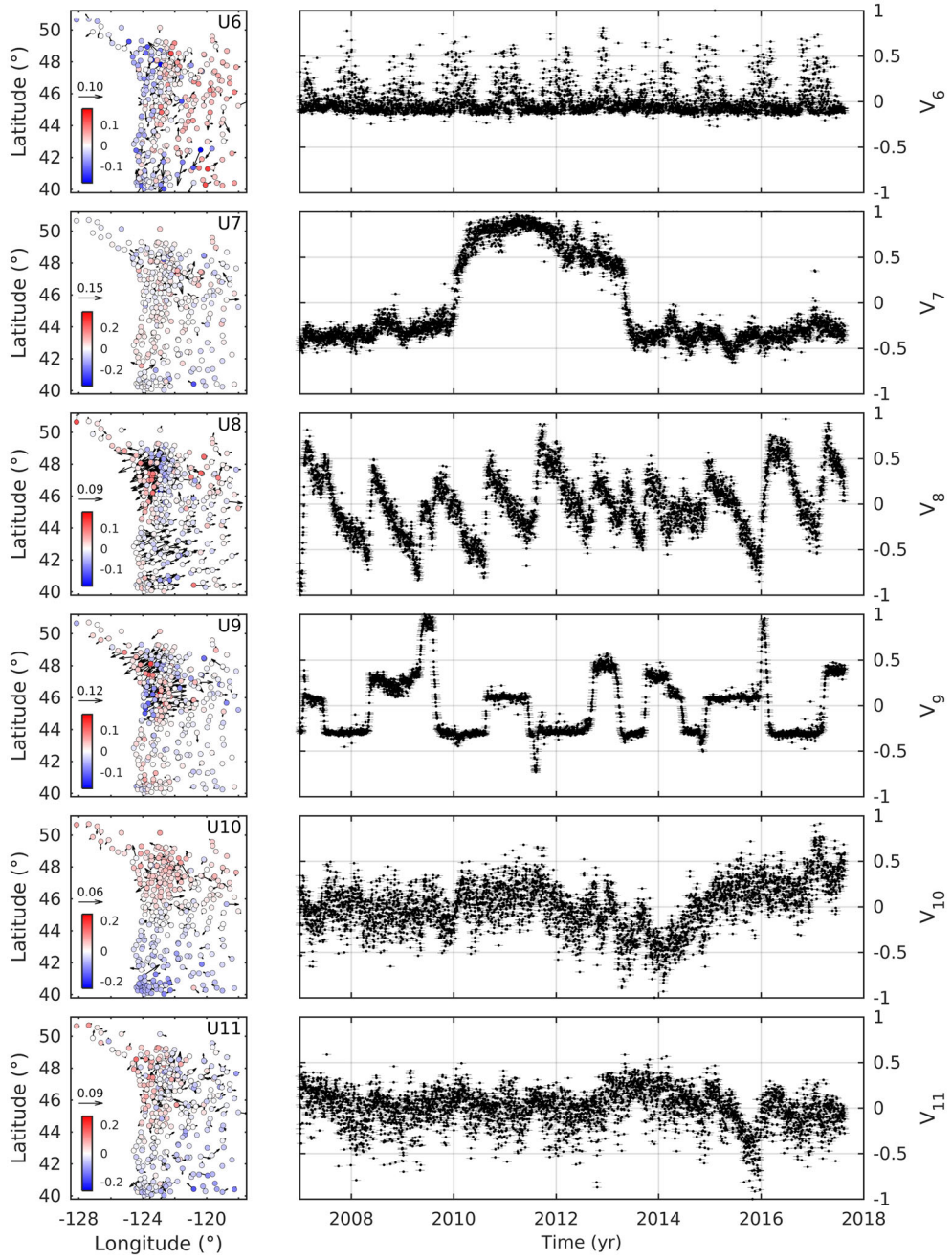


Figure 4 continued

quantities are organized in matrices, such that the following approximation holds (Gualandi et al. 2016):

$$X_{M \times T} \approx U_{M \times R} S_{R \times R} V_{R \times T}^T + N_{M \times T} \quad (1)$$

where U and V have unit norm columns, S is a diagonal matrix, and N characterizes the noise, assumed to be Gaussian. Recall $M = 3 \times N_{\text{GPS}}$ is the total number of time series (East, North, and Vertical direction per each station) and $T = 3883$ is the total number of observed epochs. This notation is similar to that of Principal Component Analysis (PCA), but here the constraint of orthogonality between the columns of U is relaxed, as well as between the columns of V . Moreover, any ICA algorithm is not aiming at the diagonalization of the variance–covariance matrix of the data and, thus, the diagonal values in S do not represent a percentage of the dataset variance explained. Both U and V are non-dimensional, while S and N are in the same unit as X (mm). In contrast to standard ICA algorithms (e.g. FastICA, Hyvarinen and Oja, 1997), vbICA allows for more flexibility in the description of the temporal sources V since it can model multimodal time function distributions. More details can be found in Gualandi et al. (2016) and references therein.

3.1.2 Post-seismic Relaxation

The largest deformation signal in the corrected position time series is due to post-seismic relaxation following the earthquakes listed in Table 1.

Due to the complexity of the tectonically active region in the proximity of northern Vancouver island in the North and of the triple junction point in the South (Table 1), it is challenging to obtain a clean source separation using the data from the entire network of stations. A first attempt to apply the vbICA to the whole dataset did not bring a clean separation between post-seismic events occurring at the northern and southern edges of the subducting plate. We, therefore, decided to first divide the study area into two sectors, split by the latitude 45° and limited to the east by the longitude -121° , as shown in Fig. 1a.

We run a first vbICA on each section to extract the post-seismic deformation, and we retrieve 8 and 6

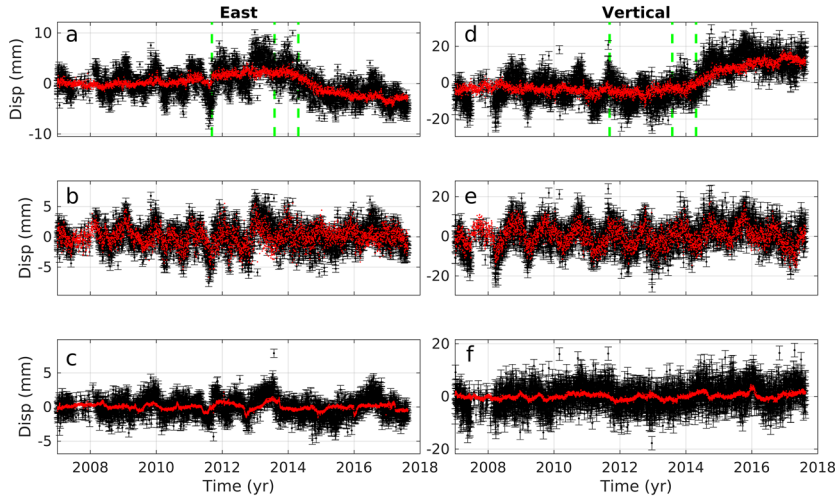
ICs for the northern and southern section, respectively (Figs. 2 and 3). The amount of variance explained by the decomposition is over 68.27%, considered here as a threshold for the selection of the number of components to be retained. For the southern section, we interpret IC1 and IC2 as related to post-seismic deformation in the region. The temporal functions show clear non-linear patterns starting at the time of occurrence of the large earthquakes (Fig. 3). Moreover, their spatial functions (U) show a signal localized in the southwestern section, in the proximity of the earthquake epicentres. The same argument is valid for the analysis of the northern section, where IC1 and IC2 are interpreted as post-seismic sources (Fig. 2). We admit that we cannot isolate the contribution of every single post-seismic deformation episode, and certainly there is cross-talk between the post-seismic ICs. Nonetheless, due to the spatially localized responses, we are confident that the information thus extracted is referring to the post-seismic deformation.

In the South, six $M5.5 +$ events (Table 1) have visibly induced detectable geodetic signals (stars in Fig. 1a and green lines in Fig. 3) and all are strike-slip events (USGS). In the North, similarly, three strike-slip $M5.5 +$ earthquakes have occurred and affected GPS stations (Table 1, Figs. 1a, 2). There is one $M7.8$ with a reverse mechanism that occurred in 2012 (Table 1, star out of frame in Figs. 1a and 2), which might have induced post-seismic deformation on the megathrust or on a crustal fault of the North American plate (Hayes et al. 2017). The mainshock occurred 363 km from the closest GPS station (HOLB). Its rupture extended $\sim 100\text{--}150$ km along strike. This event seems to have affected the northernmost stations. In either case, we make a distinction between afterslip and SSEs and thus correct our dataset X for the displacement associated with all the retrieved post-seismic ICs. The stations corrected for post-seismic deformation are listed in Table S1.

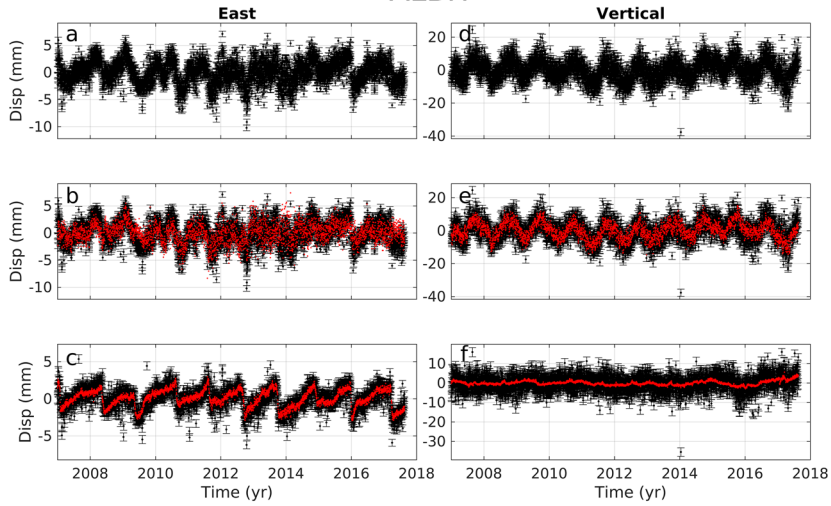
3.1.3 Seasonal Deformation

After the removal of post-seismic deformation, the largest source of deformation is due to seasonal effects. Several mechanisms can be at the origin of seasonal deformation, but the strongest is related to

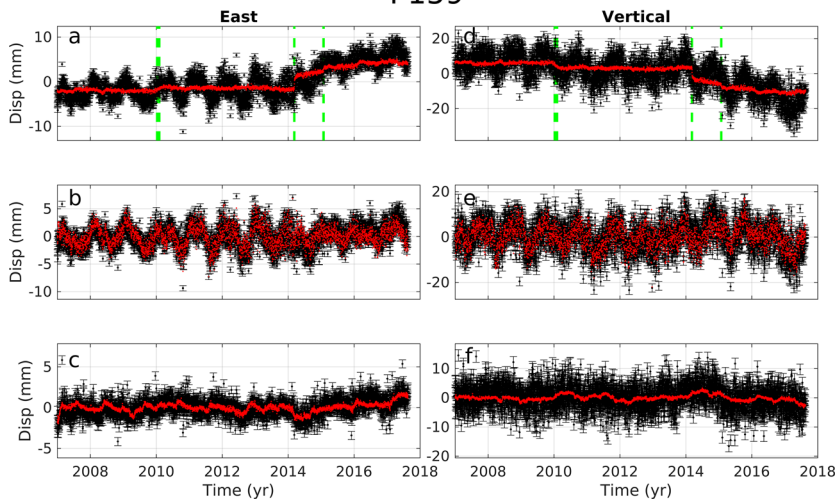
ELIZ



ALBH



P159



◀Figure 5

Comparison between the corrected GPS time series used as input for the vbICA decomposition and the modelled signal for station ELIZ, ALBH and P159, at each correction step (Sects. 3.1.2., 3.1.3. and 3.1.4.). The left and right panels indicate the East and vertical directions of the GPS time series, respectively. For each station, **a** and **d** show the detrended GPS time series (black dots and associated errorbars) and the displacement modelled from the ICs related to post-seismic deformation (red line). **b** and **e** show the detrended GPS time series corrected from post-seismic displacement (black dots and associated errorbars) and the displacement modelled from the ICs related to noise, and seasonal and local effects deformations (red line). **c** and **f** show the detrended GPS time series corrected from noise and post-seismic, seasonal and local effects deformation (black dots and associated errorbars) and the displacement modelled from the ICs related to SSEs (red line). ALBH has no post-seismic ICA model since we did not correct any post-seismic deformation at this station

the load induced by surface mass variations (e.g. Blewitt et al. 2001; Dong et al. 2002; Bettinelli et al. 2008). Thanks to satellite gravity records from the Gravity Recovery and Climate Experiment (GRACE) (Tapley et al. 2004), it is possible to estimate the load in equivalent water thickness (EWT). From this dataset, and assuming a certain composition of the

Earth, it is possible to model the predicted seasonal deformation due to this source (e.g. Chanard et al. 2014, 2018). We perform a vbICA on both the GPS position time series and the deformation predicted from the GRACE data at the same locations (Fig. 4). From the GPS decomposition, we identify components 1, 2 and 3 as seasonal sources of deformation. A decomposition with 3 ICs on the GRACE-derived time series explains 100% of the variance. A comparison of the temporal evolution of the GPS-derived and GRACE-derived ICs shows a good correlation ($> 60\%$) between the first GPS-derived and GRACE-derived components (Fig. 4) (Table S2). We conclude that the first GPS-derived component is most likely associated with hydrological loading. The other two seasonal GPS-derived components have poor correlations with any GRACE-derived component and thus cannot be interpreted as related to surface hydrology. Their origin is unknown and might be due to other seasonal non-tectonic effects here not taken into account [e.g. thermal strain (Xu et al. 2017)]. Given the uniform spatial pattern of ICs

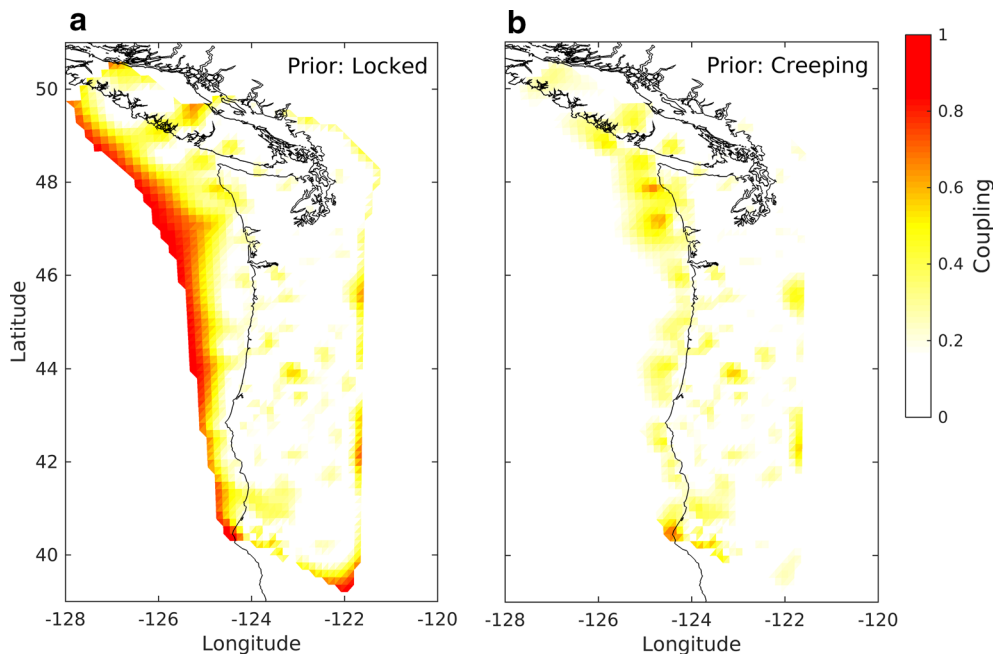


Figure 6

Interseismic coupling maps obtained with different a priori hypothesis on fault coupling. Interseismic coupling is defined as the ratio of the slip rate deficit derived from the modelling of interseismic geodetic strain over the long-term slip rate on the megathrust predicted by the block model. **a** The megathrust is assumed fully locked a priori. **b** The megathrust is a priori assumed to be creeping at the long-term slip rate. The black line corresponds to the coastline

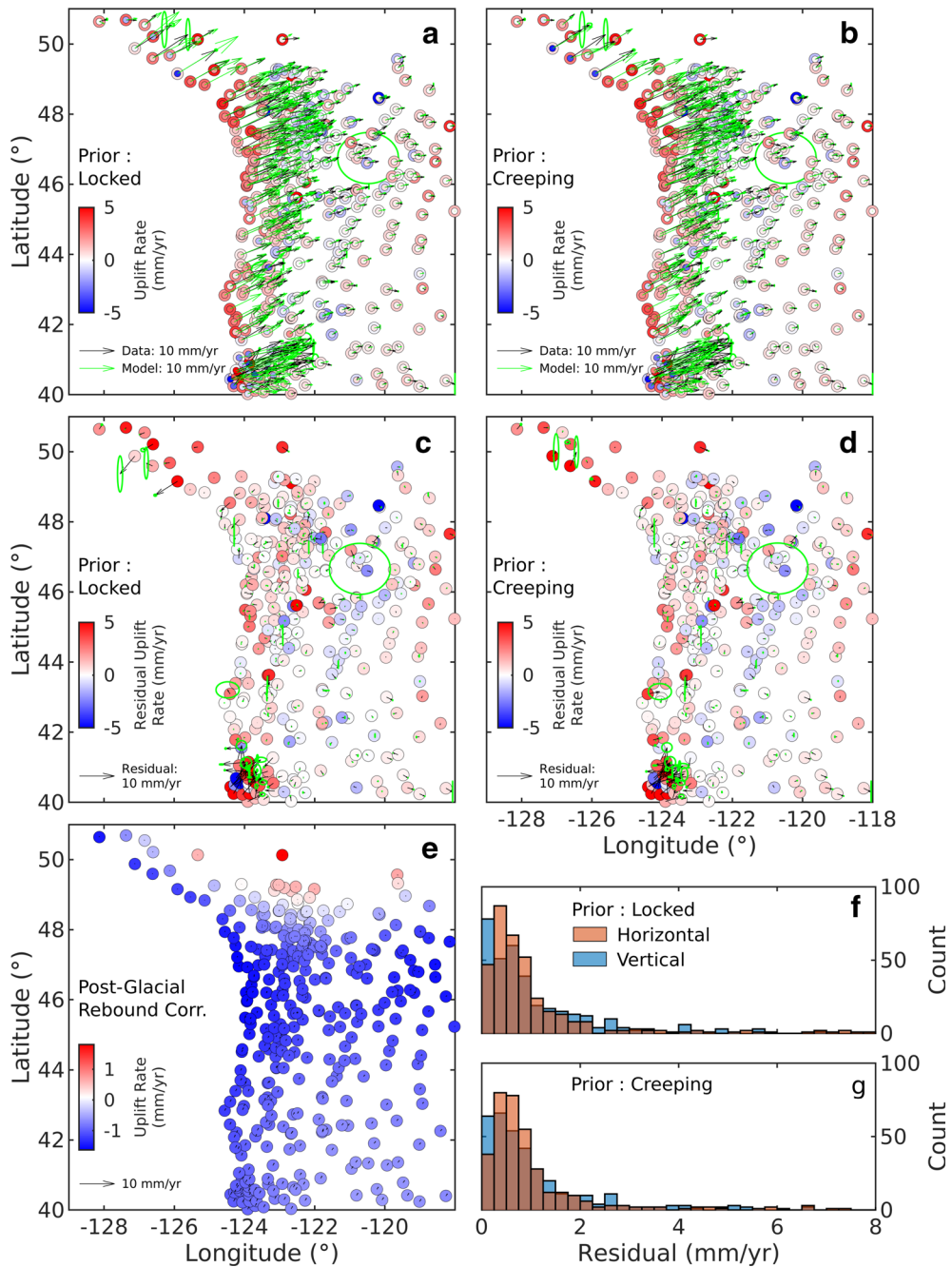


Figure 7

a and **b** show the comparison between the observed and modelled secular rates for the models assuming a priori that the megathrust is locked and creeping, respectively. **c** and **d** show the corresponding residuals assuming locking or creep a priori, respectively. **e** shows the post-glacial rebound correction based on Peltier et al. (2015). The arrows and the coloured dots indicate horizontal and vertical motion, respectively. The inner and outer dots in (**a**) and (**b**) represent the data and model vertical secular rates, respectively. The green ellipses indicate 1-sigma uncertainties. **f** and **g** show histograms of the residuals assuming locking or creep a priori, respectively

4 and 5 (Fig. 4), we make the hypothesis that they are related to a network Common Mode Error (CME). IC6 (Fig. 4) can be described as a seasonal scatter, potentially due to the effect of snow and consequent multipath, and is considered as noise. The spatial pattern of IC7 (Fig. 4) is very localized and we assume that it is a local effect. The deformation related to the ICs from 1–7 is thus removed from the time series, which have at this point been corrected from inter-block motion, long-term linear tectonic motion, co-seismic and instrumental offsets, post-seismic relaxation, seasonal signals, network errors and local effect deformations.

3.1.4 SSEs Displacement

Finally, we apply a vbICA on the residual displacement time series. The SSEs signal is buried in the noise and the percentage of variance explained grows very slowly as the number of components increases. The number of components is chosen based on the Negative Free Energy (NFE) of the decomposition, which balances the fit to the data and the complexity of the model (Choudrey and Roberts 2003; Gualandi et al. 2016). The NFE indicates how close the approximating probability density function (pdf) of the hidden variables of the model is to the true posterior pdf. When the NFE reaches its maximum value, the Kullback–Leibler divergence between the aforementioned pdfs is minimum. When passing from 32 to 33 ICs the NFE decreases, and we thus select 32 components for our final decomposition (Fig. S1). Among these 32 ICs, we ascribe 15 of them to the kinematics of SSEs (components 1–15 in Fig. S2). The remaining 17 sources are considered as either noise (components 16–25) or local effects (components 26–32) (Fig. S2).

The comparison between the GPS position time series and the vbICA reconstruction at each extraction step (i.e. Sects. 3.1.2., 3.1.3. and 3.1.4.) is shown in Fig. 5 for the 3 stations indicated in Fig. 1.

4. Interseismic Coupling

We perform a static inversion of the velocity field estimated from the trajectory model. We correct the

long-term linear trends from post-glacial rebound displacements using estimations from Peltier et al. (2015) (Fig. 7e). We use a downsampled version of the fault geometry determined by McCrory et al. (2012). The total number of sub-faults is $P = 3339$, and they have triangular shape, with a characteristic length of ~ 15 km. The Green’s functions are calculated using Okada (1992) dislocation model. We use the same regularization scheme of Radiguet et al. (2011), which allows to give an interseismic back-slip a priori model as input. Two a priori interseismic back-slip models are tested, one with a fully locked fault (coupling equal to 1), and the other with a fully creeping fault (coupling equal to 0). We expect the poorly resolved areas, specifically near the trench where no data are available, to stay near the a priori model. Those two a priori models define thus the 2 extreme cases where the fault trench is either fully locked or creeping. A rake direction constraint is imposed using the plate rate direction from Schmalzle et al. (2014) block model. We adopt as smoothing parameter the a priori uncertainty on the model parameters σ_0 , while fixing the correlation distance λ to the average patch size. Taking the locked a priori model, varying σ_0 produces the L-curve shown in Fig. S3. We select $\sigma_0 = 10^{-0.1}$ for our preferred inversion that yields the best trade-off between misfit and smoothness of the slip distribution. We use the same parametrization for the creeping a priori model. We calculate the interseismic coupling map dividing each sub-fault’s back-slip rate, given by the inversion, by its associated block model plate rate. The coupling maps for the two cases are given in Fig. 6. The fit to the data and the residuals are shown in Fig. 7. The resolution and restitution maps are shown in Fig. S4. The sensitivity to the regularisation parametrisation is shown in Fig. S5.

The two interseismic coupling maps (Fig. 6) show a partially locked shallow portion of the fault. The position of the locked zones, however, differs from one model to the other. Interestingly, the a priori fully creeping fault has locked areas that are closer to the coast than the a priori fully locked fault.

5. Slow Slip Events Kinematics

5.1. SSES Inversion

Once the surface deformations associated with the SSEs are isolated, we perform a static inversion of the spatial distribution related to the 15 extracted temporal functions. This approach follows the one adopted in Gualandi et al. (2017a, b, c). The principle is the same as the one described in Kositsky and Avouac (2010), but a vbICA is replacing the PCA decomposition of the data. We invert the selected ICs on the same geometry used for the interseismic velocities, and we adopt the same regularization scheme. A null a priori model is imposed, which implies that we expect a null a posteriori solution where the data do not require for slip on the fault. No constraints on the rake direction are imposed. Varying σ_0 produces the L-curve shown in Fig. S6. We select $\sigma_0 = 10^{-1.5}$ for our preferred inversion that yields the best trade-off between misfit and smoothness of the slip distribution. We invert the 15 ICs using the same parametrization for each IC and recombine them linearly.

We thus obtain the spatio-temporal evolution of slip deficit related to SSEs ($\delta_{\text{deficit}}(p, t)$) with respect to the long-term slip deficit given by the locking ratio (see Sect. 4). In order to get a coherent slip deficit rate ($\dot{\delta}_{\text{deficit}}(p, t)$) time evolution ($t = 1, \dots, T$) on each sub-fault ($p = 1, \dots, P$), we take the time derivative of the low-pass filtered slip deficit. In particular, we apply an equiripple low-pass filter with passband frequency of $1/21 \text{ days}^{-1}$, stopband of $1/35 \text{ days}^{-1}$, passband ripple of 1 dB with 60 dB of stopband attenuation. If the slip deficit increases on a given patch (i.e. positive slip deficit rate), then that patch is accumulating strain, i.e. it is loading. When the slip deficit decreases (i.e. negative slip deficit rate), then the patch undergoes slip. SSEs thus correspond to time periods of negative slip deficit rate. A movie of the SSEs kinematics is available in the supplement (Movie S1). The sensitivity of the kinematic model to the regularisation parametrisation is also shown in the supplement (Movie S2, S3 and S4).

Figure 8

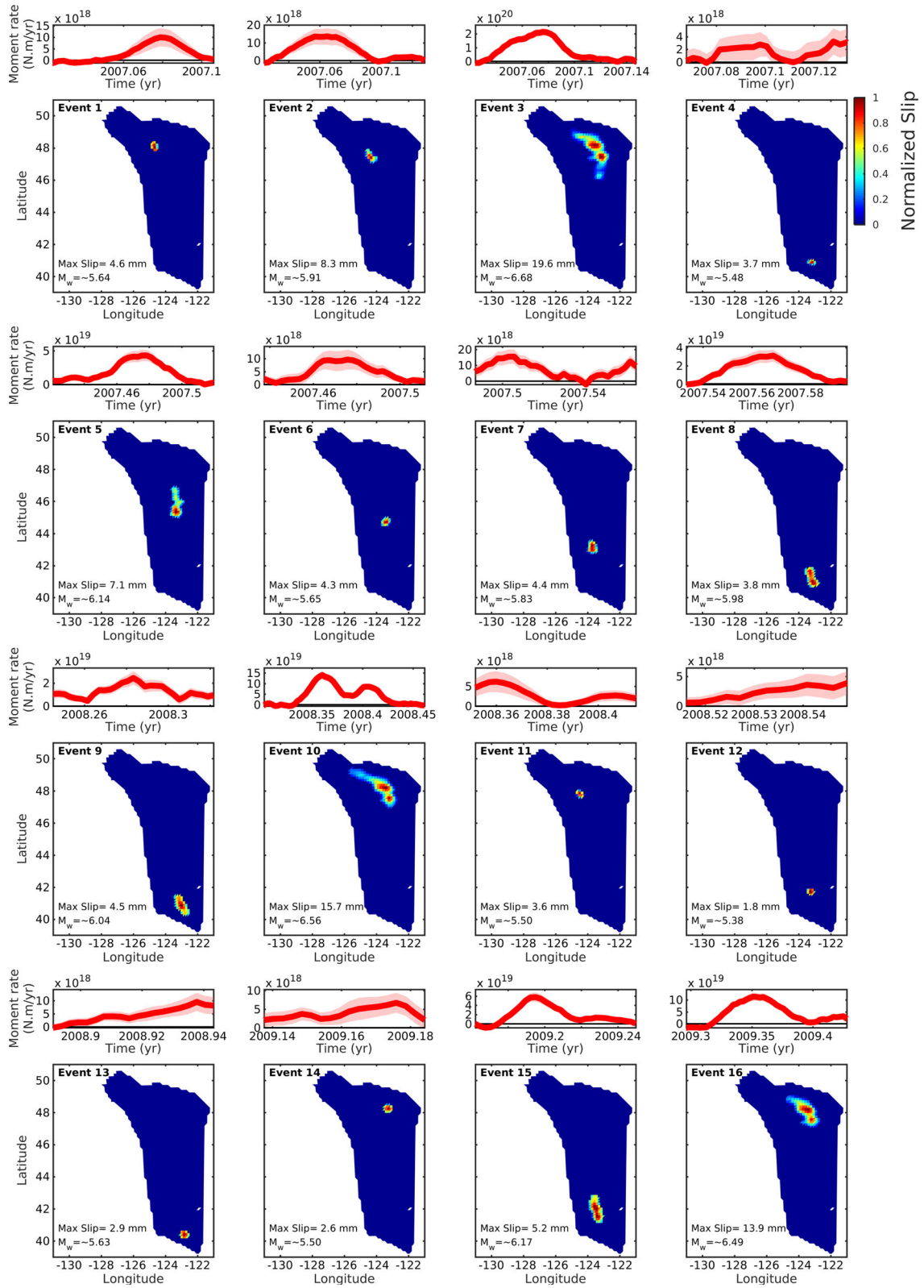
Catalogue of 64 detected SSEs which occurred between 2007 and 2017. The bottom panels indicate the normalized slip distribution of each SSEs based on the initial low-pass filtering of δ_{deficit} with a cutoff at 21 days^{-1} . The top panels with the red curve indicate their moment rate functions based on the δ_{deficit} 8-days window smoothing. The pink shading represents the moment rate function uncertainty based on the standard deviation of the mean on the rough version of δ_{deficit} using a 16-days moving window centered in the epoch of interest

5.2. SSEs Spatial and Temporal Determination

To isolate each SSE in space and time, we proceed as follows. We consider only periods where slip deficit rate is negative, thus, associated with the SSEs unloading. To enable the detection of SSEs over the noise level of our kinematic model, we make the hypothesis that at a given epoch t a given sub-fault p is experiencing an SSE if $\dot{\delta}_{\text{deficit}}(p, t) < V_{\text{thresh}} = -40 \text{ mm/year}$. For the specific epoch under exam, we identify all the sub-faults with slip rates below this threshold by applying a contour at V_{thresh} . The number of contours defines the number of SSEs occurring at time t . We do the same at time $t + 1$ and verify which contours at time $t + 1$ overlap with the contours at time t . If there is an overlap, we assume that they are the same SSE. For every SSE, we thus automatically select a starting and ending time (t_k^{in} and t_k^{fin} , with $k = 1, \dots, N_{\text{SSEs}}$). Special cases can arise where an SSE splits itself or two SSEs merge together. In both scenarios, the SSEs at time t and $t + 1$ are considered to be the same. With this procedure, we identify 119 potential SSEs between 2007 and 2017. From those 119, some involve only 1 or 2 sub-faults and are very short in time. We consider them as noise. We also remove any candidate under 60 km depth. Our final selection of SSEs gathers $N_{\text{SSEs}} = 64$ events shown in Fig. 8.

With this procedure, we are able to estimate the temporal and spatial evolution of each SSE. To get their moment rate function, we proceed as follows. Since SSEs can migrate, we estimate the full area involved in the k -th event as the union of all the sub-faults participating to it, denoted by the set $\{s_k\} = \left\{ p \mid \dot{\delta}_{\text{deficit},k}(p, t) < V_{\text{thresh}} \text{ for } t_k^{\text{in}} \leq t \leq t_k^{\text{fin}} \right\}$. However, the V_{thresh} parameter might truncate

Interseismic Coupling and Slow Slip Events on the Cascadia Megathrust



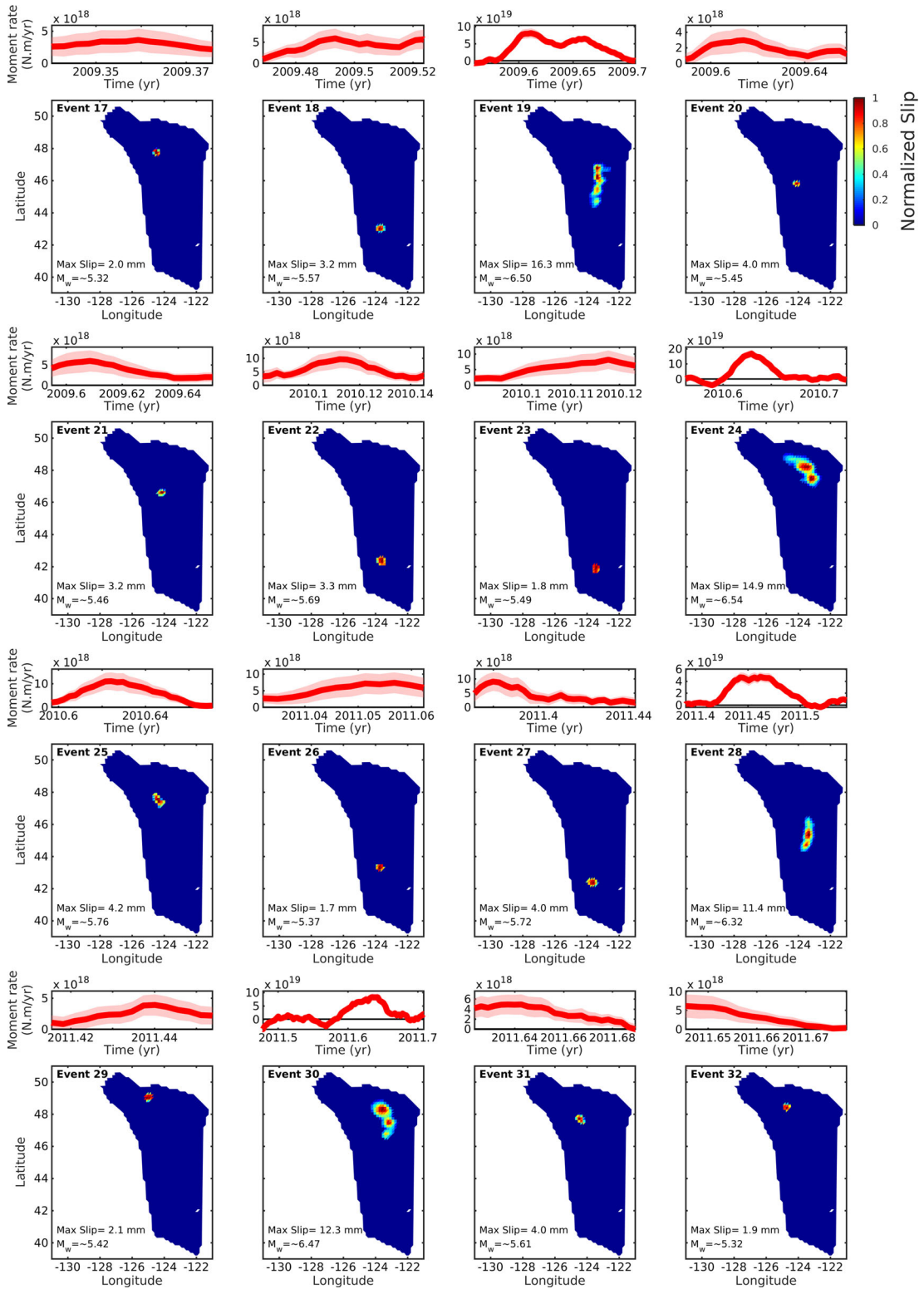


Figure 8 continued

Interseismic Coupling and Slow Slip Events on the Cascadia Megathrust

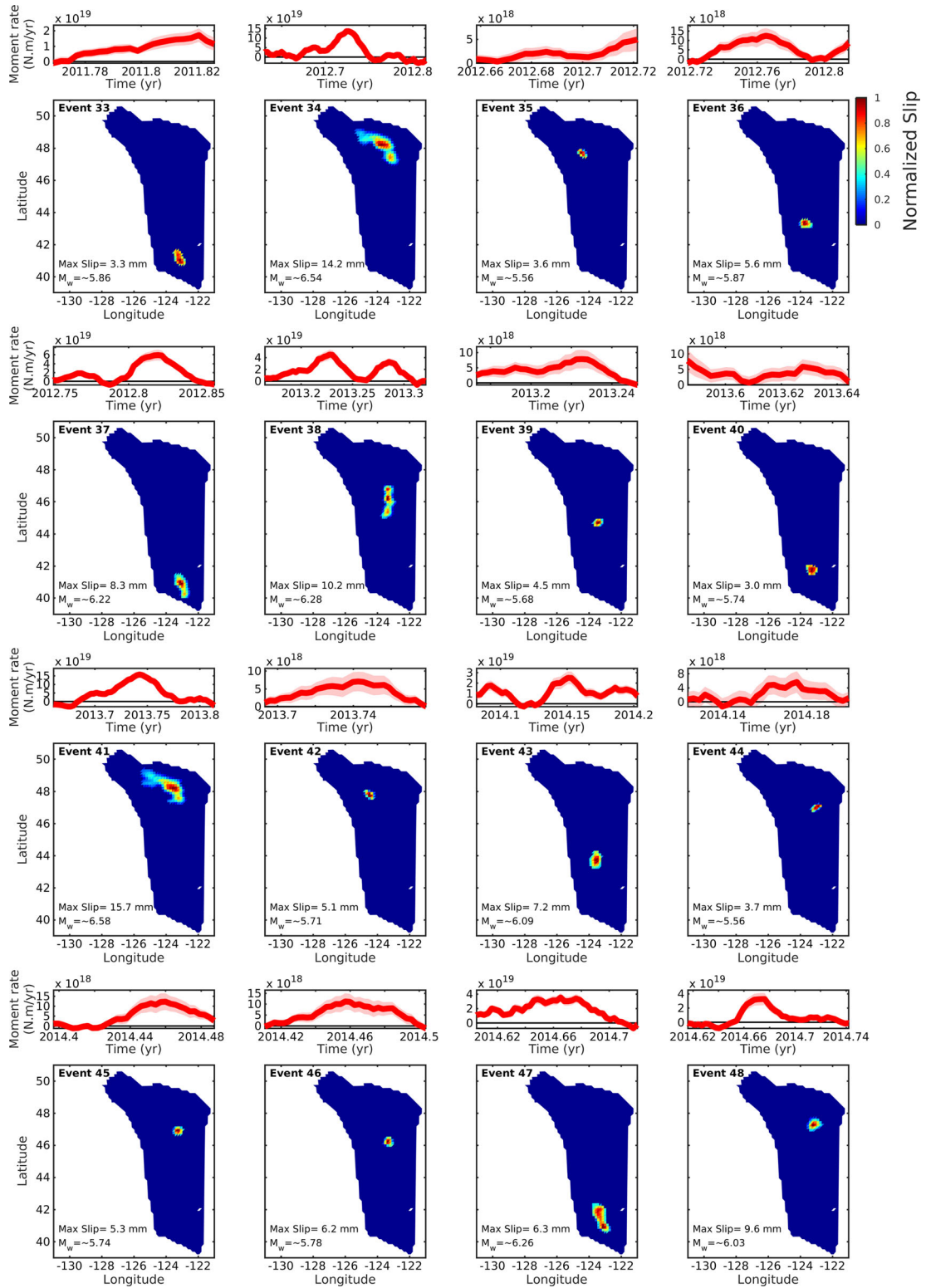


Figure 8 continued

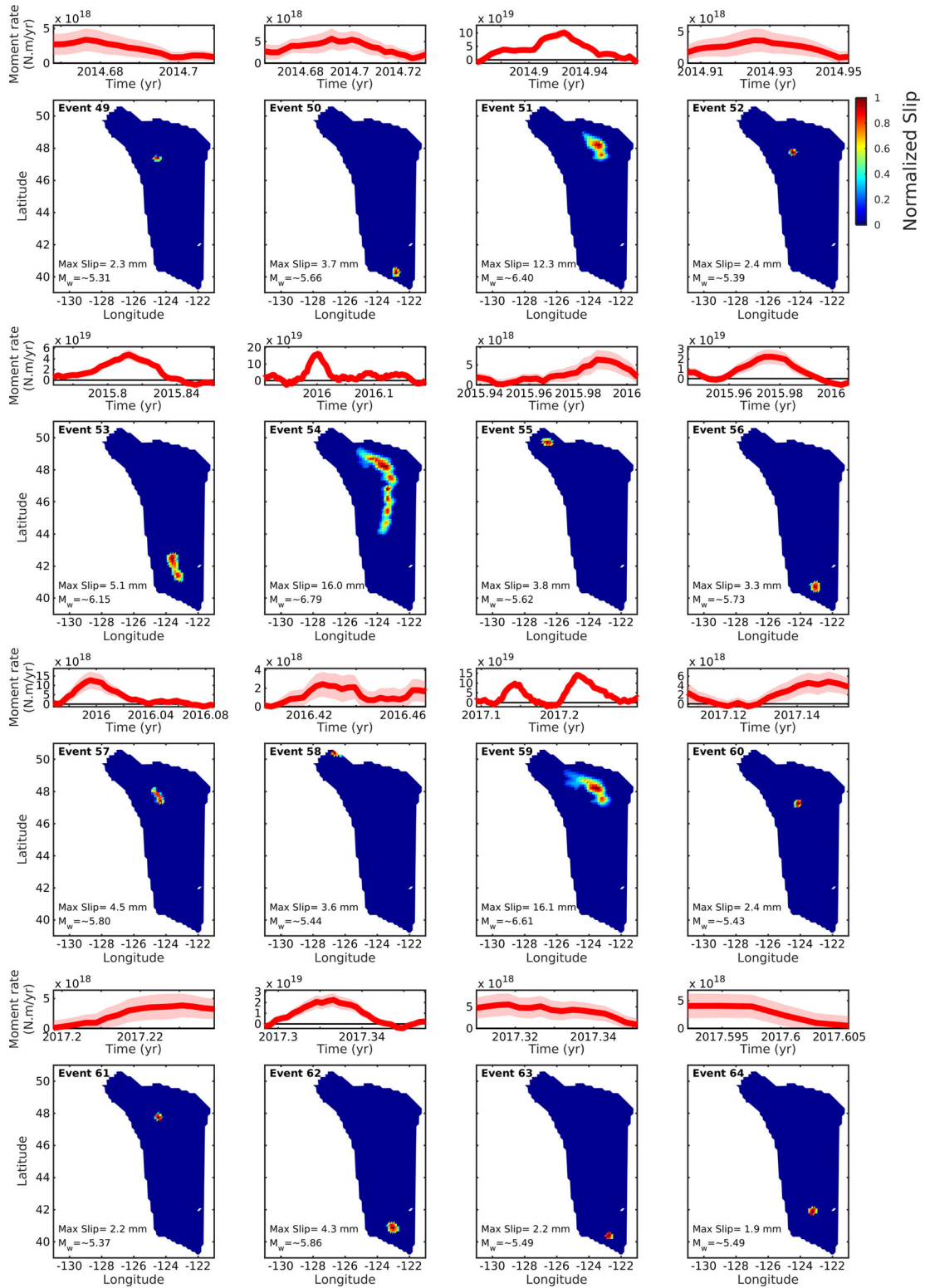


Figure 8 continued

spatially and temporally our estimated SSEs. To relax slightly this constrain, we extend the spatial influence of each SSE to their neighbouring sub-faults and extend their time delimitation by 1 day before and after. Note that during and within the area of influence of each SSE, the slip deficit rate of sub-faults can be negative or positive depending on the SSE's history of propagation. For one event, within its area of influence and time period, we calculate the moment rate function at time t , $\dot{M}_0(t)$, using equation:

$$\dot{M}_{0,k}(t) = - \sum_{s_k=1}^{S_k} \mu A_{s_k} \dot{\delta}_{\text{deficit},k}(s_k, t), \quad \text{for} \quad (2)$$

$$t_k^{\text{in}} \leq t \leq t_k^{\text{fin}} \quad \text{and} \quad \text{with} \quad k = 1, \dots, N_{\text{SSEs}},$$

where μ is the shear modulus (here fixed to 30 GPa), S_k is the total number of sub-faults belonging to the k -th SSE's area of interest, A_{s_k} is the area of sub-fault s_k . The negative sign in front of the sum is added in order to have positive moment rates during SSEs, reference that we will keep for the rest of this study.

Applying this moment rate calculation methodology on the filtered δ_{deficit} described in Sect. 5.1 (passband frequency of $1/21 \text{ days}^{-1}$, stopband of $1/35 \text{ days}^{-1}$) results, however, in very smoothed moment rate functions. To retrieve more detailed moment rate functions, we perform instead a zero-phase digital filtering on the rough δ_{deficit} using a 8-days window, but focus only on the area and time period of each SSE as estimated before from the very smoothed data. The moment rate of each SSE acquired from the rougher version of δ_{deficit} is shown in Fig. 8. Those moment rates do not take into account interseismic loading during SSEs. To estimate the uncertainty on the SSEs moment rate function, we assume that it is represented by their short-term variability before filtering. The uncertainties represented in Fig. 8 are calculated based on the standard deviation of the mean on the rough version of δ_{deficit} using a 16-day moving window centered in the epoch of interest.

To evaluate SSEs propagation speed from our kinematic model, we estimate SSE propagation front locations as follows. A representative line of the average along-strike location of SSEs is first chosen (red line in Fig. 9a, Table S3). The intersection between this line and the contour of the cumulative

slip area of SSEs at each time step ($\dot{\delta}_{\text{deficit}} < V_{\text{thresh}}$) defines the position of the SSE propagation fronts. The distance, along the SSEs location representative line, between the propagation fronts and the onset location of each SSE is then calculated at each time step. The onset location of SSEs is assumed to be the projected barycentre of their first slip area contour on the SSE location representative line. Figure 9 shows the position of 14 SSEs front as a function of time.

5.3. SSEs Kinematics

Our SSE catalogue (Fig. 8) contains events with moment magnitude from 5.3 to 6.8 and duration between 14 and 106 days. Their propagation speed is of the order of $\sim 2000\text{--}4000 \text{ km/year}$ (respectively, $\sim 5.5\text{--}11 \text{ km/day}$) (Fig. 9).

The spatio-temporal evolution of the tremors and SSEs is systematically correlated (Movie S1) as shown for example for event 34 in Fig. 10, as had already been shown in some previous studies (Wech and Bartlow 2014). The SSEs located slightly offshore, along the coast between 47° and 49° of latitude (e.g. events 1, 2), are most likely inversion artefacts, since a limited number of stations are present in the offshore portion of the megathrust.

From our catalogue (Figs. 8 and 11c), we observe that SSEs often rupture the northern (i.e. event 10, 16, 24, 34, 41, 51, and 59), centre (i.e. events 5, 19, 28 and 38) or southern (i.e. events 8, 9, 15, 33, 37, 47 and 53) segments of Cascadia independently, but sometime multiple segments are ruptured during a single event (i.e. event 54). Segments are thus not completely independent from one another (Schmidt and Gao 2010; Wech and Bartlow 2014). We also observe that SSEs can rupture segments from either North to South or South to North, showing that the direction of propagation is variable (Schmidt and Gao 2010). Some events propagate also bilaterally (Schmidt and Gao 2010; Dragert and Wang 2011; Wech and Bartlow 2014) as is observed for the event 24 in our inversion (Movie S1).

The combined moment rate of all the SSEs from our catalogue between 2007 and 2017 is shown in Fig. 11a. Two endmembers are shown, one assuming that interseismic loading is negligible during SSEs and the other assuming that the fault is loaded at the

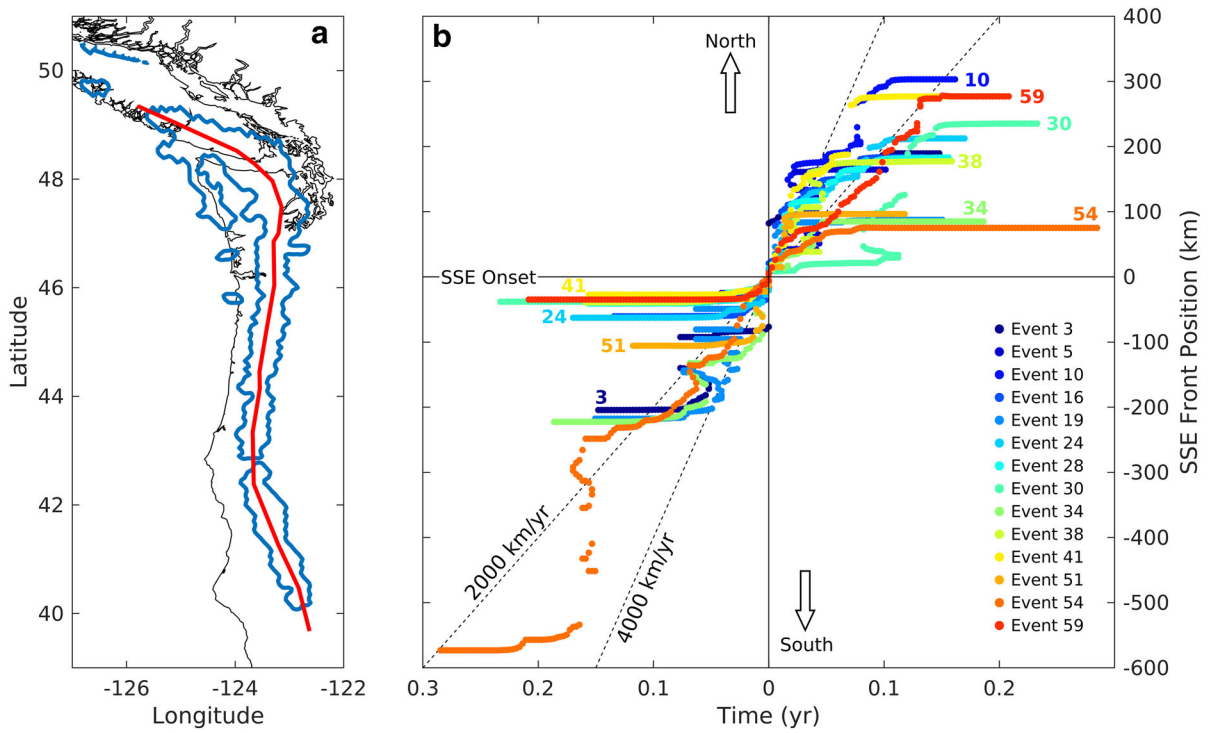


Figure 9

SSE front position evolution of 14 events. **a** Map showing the representative line of the average along-strike location of SSEs (red line). The intersection between this line and the SSEs cumulative slip contour at each time step indicates location of the SSEs fronts. The blue line indicates the cumulative slip area contour of all SSEs. The black lines indicate the coast. **b** SSEs front positions as a function of time in reference to the SSEs onset locations. Positive position is to the North, negative to the South. Time axes are symmetric (positive on both sides), recording the time after the SSE onset. The two green dashed lines are reference propagation rates of 2000 (~ 5.5 km/day) and 4000 km/year (~ 11 km/day)

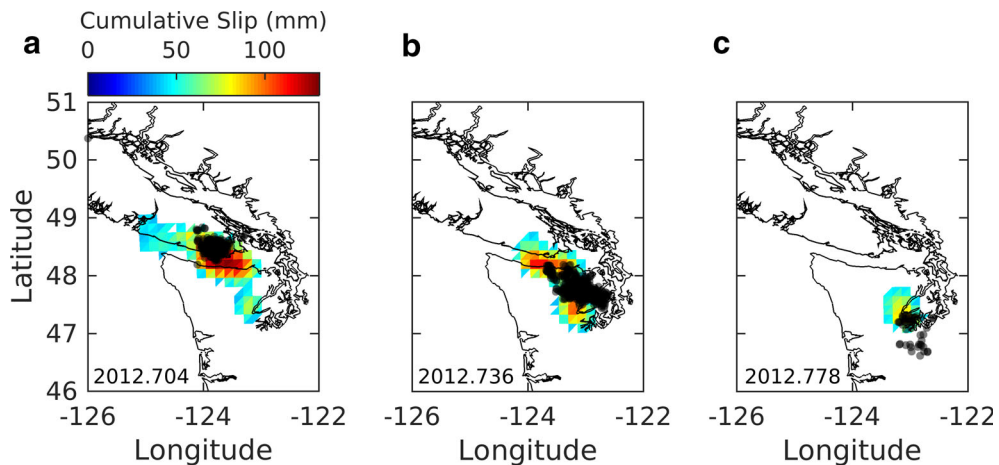


Figure 10

Three snapshot of the slip cumulated over 1 day during the propagation of SSE 34. The black dots correspond to tremors for the same days. The black lines indicate the coast. The bottom left number corresponds to the date. The tremors closely track the propagation of the SSE

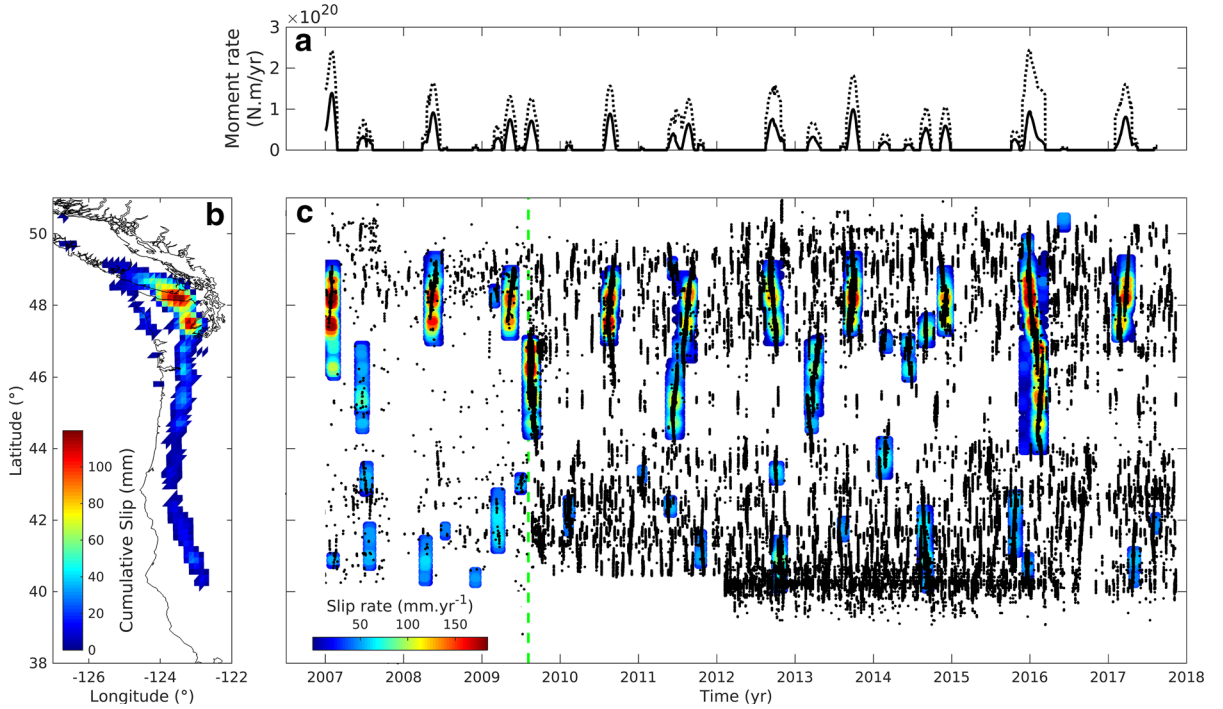


Figure 11

a Combined moment rate functions of all the detected SSEs from our catalogue. The continuous and dashed black lines correspond to the moment rate taking and without taking into account interseismic loading during SSEs, respectively. To place an upper bound on the moment release during SSEs, the dashed lines are calculated by comparison with the moment deficit that would have occurred during each SSE had the fault remained fully locked. Those moment rate functions are based on the low-pass filtered δ_{deficit} with the passband at 21 days^{-1} . **b** SSEs cumulative slip. **c** Occurrence of SSEs (colour shading) as a function of time. The black dots indicate tremors. The catalogue from Ide (2012) is used until 2009.595, the catalogue from PNSN is used thereafter

long-term plate rate during this period. They represent the two possible extremes of moment rate released by the SSEs from our catalogue. Bias in segment determination is introduced from the selection of V_{thresh} . For example, certain SSEs might not be detected or a same SSE could have been cut into pieces (e.g. events 28 and 30 in 2011). Increasing V_{thresh} to -35 mm/year , we retrieve instead 81 SSEs, several events are merged (events 1,2 and 3 in 2007 or 28 and 30 in 2011), smaller events appear, but the global dynamics remains unchanged (Fig. S7). Additionally, increasing V_{thresh} also increases the risk of introducing noise.

5.4. Potential Biases and Limitations

The combination of the uncertainty on GPS measurements, the low-pass filtering, the value of V_{thresh} and the interpreted fault geometry, specifically in the North, hinders our possibility to retrieve small

SSEs that remains within the noise level. In the most Northern part of the fault, our kinematic model is difficult to interpret due to the proximity of the fault's border which is prone to noise from the inversion. The southern part of Cascadia seems more prone to having small SSEs, which are more difficult to detect. This can be due to the slower convergence rate of the region (27 mm/year) compared to the northern segments (45 mm/year). The spatial distribution of GPS stations plays also a role in that matter.

Two opposite effects may affect the duration estimation of the SSEs. The temporal slip deficit filtering tends to augment SSEs duration. On the other hand, the selection of small enough (i.e. large enough in absolute value, in order to limit the effects of noise) V_{thresh} cuts the onset (t_k^{in}) and end (t_k^{fin}) of SSEs. Moreover, it additionally impacts SSEs' spatial extent, disregarding areas that do not slide fast enough. The value of the estimated peak slip during an SSE (Fig. 8) depends on the regularization of the

inversion. The fact that the inversions are ill-posed and require regularization thus probably explains why different inversions can yield significantly different peak slip values. For example, the SSEs peak slip reported in our study (~ 1.5 cm) are smaller than the peak slip indicated in Dragert and Wang (2011) ($\sim 3\text{--}5$ cm) for the May 2008 event.

There is also a possibility that the number of selected ICs used for the SSE model (Sect. 3.1.4) biases the kinematic description. In our case, 15 components were selected to describe the kinematics. However, the selection is initially based on a pool of 32 components with 17 components seemingly noise. Increasing or decreasing the total number of components produced by the vbICA changes slightly the number of ICs related to SSEs, but does not change qualitatively the dynamics observed in our model. On the contrary, by increasing the total number of ICs, the vbICA extracts further components estimated as local effects or noise. We tested up to 44 ICs.

The uncertainty on the position of the SSEs propagation front also depends on the factors mentioned above (i.e. GPS measurements, low-pass filtering, value of V_{thresh} , interpreted fault geometry and number of ICs). Additionally, the choice of the representative line of the average along-strike location of SSEs also plays a role, even though minor. Note that the initial phase of the SSEs front positions might represent more a shadow of the slip deficit rate of SSEs decreasing under V_{thresh} rather than the actual SSEs front propagation. The values of SSE front propagation rate estimated from our kinematic model are anyways similar to the ones estimated from tremor propagation since SSEs and tremors are most often correlated.

6. Implications and Conclusion

We determined the secular model of interseismic coupling on the megathrust (the time-average pattern of locking ratio) and the kinematics of SSEs from 2007 to 2017 in a consistent and coherent way. The vbICA has shown to be very effective at separating the SSEs from the various other sources of temporal variations in the position time series, such as those due to surface hydrology, post-seismic signals, local effects or common mode motion.

With our vbICA-based Inversion Method (vbICA-IM), we were therefore able to describe the kinematics of fault slip on the Cascadia megathrust between 2007 and 2017 using 352 cGPS position time series. Our kinematic model provides the most comprehensive view of the SSEs along Cascadia. We were able to produce a catalogue of 64 events over the 2007–2017 time period. As already documented in previous studies of SSEs (e.g. Bartlow et al. 2011; Wech and Bartlow 2014), we find a remarkable systematic correlation in space and time between SSEs and tremors.

Our analysis demonstrates a clear along-dip segmentation of the mode of slip along the megathrust (Fig. 12). Some locked zone is clearly needed

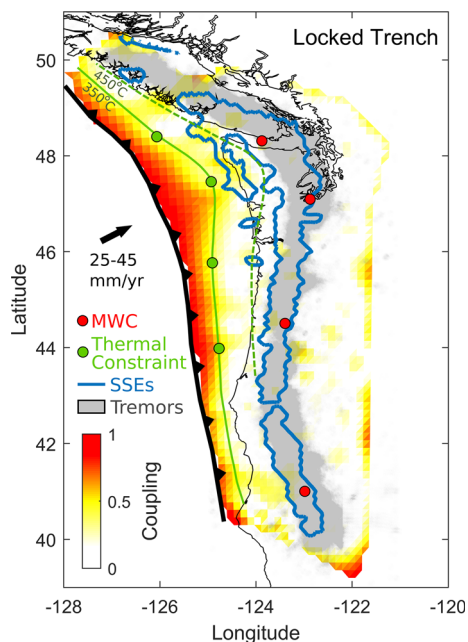


Figure 12

Interseismic coupling (white to red shading) and tremor (grey dots) distribution. The thin black curve indicates the coast. The blue contour indicates the area influenced by SSEs as measured in this study. The red dots indicate the position of the intersection between the forearc Moho and the megathrust, so the tip of the mantle wedge corner (MWC), determined from geophysical profiles along which dV_s/V_s and V_s was determined (POLARIS at the southern tip of the Vancouver Island (Nicholson et al. 2005), CASC93 in central Oregon (Nabelek et al. 1996; Rondenay et al. 2001), CAFE at Puget Sound (McGary et al. 2011; Abers et al. 2009), and FAME, BDSN and USArray/TA in the south of Cascadia). The solid and dashed green lines indicate the location of the 350 and 450 °C isotherms on the megathrust (Hyndman et al. 2015). The green dots represent the location of thermal constraints used to estimate the isotherms

between the trench and the coastline to account for the secular compression and the secular pattern of subsidence and uplift (Fig. 7). The resolution near the trench is poor and we cannot determine if the locked zone extends all the way to the trench or not. The models obtained assuming either a priori creep or locking of the megathrust fit the data equally well. They yield somewhat different position of the downdip limit of the locked zone (Fig. 6). It lies about $\sim 20\text{--}80$ km updip of the coastline at a depth of about $\sim 5\text{--}15$ km when the megathrust is assumed locked a priori (Fig. 6a). It lies much closer to the coastline, corresponding to a depth of about $\sim 10\text{--}30$ km, if the megathrust is assumed to be creeping a priori (Fig. 6b). These observations are consistent with most previous studies of interseismic coupling (e.g. Wang et al. 2001; McCaffrey et al. 2000, 2007; Bruhat and Segall 2016). The portion of the megathrust that ruptures during large interplate earthquakes must lie mostly updip of such transition between locked and creeping sections. The lack of seismicity over the transition zone hints for a fully locked shallow portion of the fault (Wang and Trehu 2016). We would also expect earthquakes to nucleate along the zone of stress accumulation, at the transition between the locked and creeping region, as is observed for example in the context of other megathrusts (e.g. Cattin and Avouac 2000; Bollinger et al. 2004). The lack of seismicity in this zone where stress is accumulating the fastest is intriguing. It suggests that the interseismic stress buildup has not yet compensated the last stress drop event to trigger earthquakes there. It could also suggest that large interplate earthquakes penetrate deeper than the lower edge of the locked fault zone. Jiang and Lapusta (2016) demonstrated via numerical simulations of the seismic cycle under a rate-and-state friction framework that this mechanism would indeed produce a protracted period of seismic quiescence.

The zone of SSEs and tremors is relatively well resolved and, when compared with the interseismic coupling model (Fig. 12), clearly reflects a downdip segmentation of the mode of slip on the megathrust. This zone lies inland from the coastline and is clearly disconnected from the locked zone as already pointed out in some past studies (e.g. Gao and Wang 2017). In this transition zone, which spans between ~ 100

km and ~ 150 km away from the trench, fault creep is remarkably stationary resulting in a slip rate close to the long-term slip rate along the megathrust. This zone thus seems to act as a buffer isolating the seismogenic zone of the megathrust from the zone of SSEs. This buffering zone probably reduces the risk that an SSE triggers a large megathrust rupture (Segall and Bradley 2012).

The downdip segmentation of the mode of slip along megathrust has long been noticed and considered to reflect the influence of both temperature and lithology (Hyndman et al. 1997; Scholz 1998; Oleskevitch et al. 1999). These two factors could also explain the existence of two separate zones of unstable frictional sliding (Gao and Wang 2017). The one closer to the trench would correspond to a zone of rate-weakening frictional sliding controlled by the frictional properties of continental rocks. For quartzo-feldspathic rocks, friction indeed transitions from rate-weakening to rate-strengthening as temperature exceeds ~ 350 °C (Blanpied et al. 1995). In Cascadia, this temperature is reached at a depth shallower than the intersection with the forearc Moho, and therefore probably determines the downdip limit of the shallower zone of unstable sliding (Hyndman et al. 1997; Scholz 1998; Oleskevitch et al. 1999) (Fig. 12). The second region is instead located around the mantle wedge corner, where high-pore fluid pressure might result in low permeability of the serpentinized mantle (Wada et al. 2008). This hypothesis is consistent with the correlation between the zone of SSEs and tremors with the forearc Moho (red dots in Fig. 12) as proposed by Gao and Wang (2017).

Acknowledgements

We thank Kelin Wang for his constructive review of this manuscript. This study was partially supported by NSF award EAR-1821853 to JPA. We thank also Zachary E. Ross for his help. We thank Kristel Chanard for discussions and providing the times series predicted based on the surface mass variations derived from GRACE.

Open Access This article is distributed under the terms of the Creative Commons Attribution 4.0 International License (<http://creativecommons.org/licenses/by/4.0/>), which permits unrestricted

use, distribution, and reproduction in any medium, provided you give appropriate credit to the original author(s) and the source, provide a link to the Creative Commons license, and indicate if changes were made.

REFERENCES

- Abers, G. A., MacKenzie, L. S., Rondenay, S., Zhang, Z., Wech, A. G., & Creager, K. C. (2009). Imaging the source region of Cascadia tremor and intermediate-depth earthquakes. *Geology*, *37*(12), 1119–1122.
- Atwater, B. F. (1987). Evidence for great Holocene earthquakes along the outer coast of Washington State. *Science*, *236*(4804), 942–944.
- Atwater, B. F., & Hemphill-Haley, E. (1997) *Recurrence intervals for great earthquakes of the past 3,500 years at northeastern Willapa Bay, Washington* (No. 1576). Washington, D.C.: USGPO.
- Bartlow, N. M., Miyazaki, S. I., Bradley, A. M., & Segall, P. (2011). Space-time correlation of slip and tremor during the 2009 Cascadia slow slip event. *Geophysical Research Letters*, *38*(18), 1–6.
- Bettinelli, P., Avouac, J. P., Flouzat, M., Bollinger, L., Ramillien, G., Rajaure, S., et al. (2008). Seasonal variations of seismicity and geodetic strain in the Himalaya induced by surface hydrology. *Earth and Planetary Science Letters*, *266*(3–4), 332–344.
- Blanpied, M. L., Lockner, D. A., & Byerlee, J. D. (1995). Frictional slip of granite at hydrothermal conditions. *Journal of Geophysical Research-Solid Earth*, *100*(B7), 13045–13064.
- Blewitt, G., Lavallée, D., Clarke, P., & Nurutdinov, K. (2001). A new global mode of earth deformation: Seasonal cycle detected. *Science*, *294*(5550), 2342–2345.
- Bollinger, L., Avouac, J. P., Cattin, R., & Pandey, M. R. (2004). Stress buildup in the Himalaya. *Journal of Geophysical Research: Solid Earth*, *109*(B11), 1–8.
- Bruhat, L., & Segall, P. (2016). Coupling on the northern Cascadia subduction zone from geodetic measurements and physics-based models. *Journal of Geophysical Research: Solid Earth*, *121*(11), 8297–8314.
- Cattin, R., & Avouac, J. P. (2000). Modeling mountain building and the seismic cycle in the Himalaya of Nepal. *Journal of Geophysical Research: Solid Earth*, *105*(B6), 13389–13407.
- Chanard, K., Avouac, J. P., Ramillien, G., & Genrich, J. (2014). Modeling deformation induced by seasonal variations of continental water in the Himalaya region: sensitivity to Earth elastic structure. *Journal of Geophysical Research: Solid Earth*, *119*(6), 5097–5113.
- Chanard, K., Fleitout, L., Calais, E., Reischung, P., & Avouac, J. P. (2018). Toward a global horizontal and vertical elastic load deformation model derived from GRACE and GNSS station position time series. *Journal of Geophysical Research: Solid Earth*, *123*(4), 3225–3237.
- Chlieh, M., Avouac, J. P., Sieh, K., Natawidjaja, D. H., & Galetzka, J. (2008). Heterogeneous coupling of the Sumatran megathrust constrained by geodetic and paleogeodetic measurements. *Journal of Geophysical Research: Solid Earth*, *113*(B5), 1–31.
- Choudrey, R., & Roberts, S. (2003). *Variational Bayesian mixture of independent component analysers for finding self-similar areas in images*. Nara: ICA.
- Clague, J. J., & Bobrowsky, P. T. (1994). Evidence for a large earthquake and tsunami 100–400 years ago on western Vancouver Island, British Columbia. *Quaternary Research*, *41*(2), 176–184.
- DeMets, C., & Dixon, T. H. (1999). New kinematic models for Pacific-North America motion from 3 Ma to present, I: Evidence for steady motion and biases in the NUVEL-1A model. *Geophysical Research Letters*, *26*(13), 1921–1924.
- Dong, D., Fang, P., Bock, Y., Cheng, M. K., & Miyazaki, S. I. (2002). Anatomy of apparent seasonal variations from GPS-derived site position time series. *Journal of Geophysical Research: Solid Earth*, *107*(B4), 1–17.
- Dragert, H., & Wang, K. (2011). Temporal evolution of an episodic tremor and slip event along the northern Cascadia margin. *Journal of Geophysical Research: Solid Earth*, *116*(B12), 1–12.
- Dragert, H., Wang, K., & James, T. S. (2001). A silent slip event on the deeper Cascadia subduction interface. *Science*, *292*(5521), 1525–1528.
- Fu, Y., Freymueller, J. T., & Jensen, T. (2012). Seasonal hydrological loading in southern Alaska observed by GPS and GRACE. *Geophysical Research Letters*, *39*(15), 1–5.
- Gao, X., & Wang, K. (2017). Rheological separation of the megathrust seismogenic zone and episodic tremor and slip. *Nature*, *543*(7645), 416.
- Goldfinger, C., Galer, S., Beeson, J., Hamilton, T., Black, B., Romsos, C., et al. (2017). The importance of site selection, sediment supply, and hydrodynamics: A case study of submarine paleoseismology on the Northern Cascadia margin, Washington USA. *Marine Geology*, *384*, 4–46.
- Gualandi, A., Nichele, C., Serpelloni, E., Chiaraluce, L., Anderlini, L., Latorre, D., et al. (2017a). Aseismic deformation associated with an earthquake swarm in the northern Apennines (Italy). *Geophysical Research Letters*, *44*(15), 7706–7714.
- Gualandi, A., Perfettini, H., Radiguet, M., Cotte, N., & Kostoglodov, V. (2017b). GPS deformation related to the Mw7. 3, 2014, Papanao earthquake (Mexico) reveals the aseismic behavior of the Guerrero seismic gap. *Geophysical Research Letters*, *44*(12), 6039–6047.
- Gualandi, A., Avouac, J. P., Galetzka, J., Genrich, J. F., Blewitt, G., Adhikari, L. B., et al. (2017c). Pre-and post-seismic deformation related to the 2015, Mw7. 8 Gorkha earthquake, Nepal. *Tectonophysics*, *714*, 90–106.
- Gualandi, A., Serpelloni, E., & Belardinelli, M. E. (2016). Blind source separation problem in GPS time series. *Journal of Geodesy*, *90*(4), 323–341.
- Hayes, G. P., Meyers, E. K., Dewey, J. W., Briggs, R. W., Earle, P. S., Benz, H. M., & Furlong, K. P. (2017). *Tectonic summaries of magnitude 7 and greater earthquakes from 2000 to 2015* (No. 2016–1192). Reston: US Geological Survey.
- Hyndman, R. D., McCrory, P. A., Wech, A., Kao, H., & Ague, J. (2015). Cascadia subducting plate fluids channelled to fore-arc mantle corner: ETS and silica deposition. *Journal of Geophysical Research: Solid Earth*, *120*(6), 4344–4358.
- Hyndman, R. D., Yamano, M., & Oleskevich, D. A. (1997). The seismogenic zone of subduction thrust faults. *Island Arc*, *6*(3), 244–260.
- Ide, S. (2012). Variety and spatial heterogeneity of tectonic tremor worldwide. *Journal of Geophysical Research: Solid Earth*, *117*(B3), 1–18.
- Jiang, J., & Lapusta, N. (2016). Deeper penetration of large earthquakes on seismically quiescent faults. *Science*, *352*(6291), 1293–1297.

- Kelsey, H. M., Nelson, A. R., Hemphill-Haley, E., & Witter, R. C. (2005). Tsunami history of an Oregon coastal lake reveals a 4600 yr record of great earthquakes on the Cascadia subduction zone. *Geological Society of America Bulletin*, *117*(7–8), 1009–1032.
- Kemp, A. C., Cahill, N., Engelhart, S. E., Hawkes, A. D., & Wang, K. (2018). Revising estimates of spatially variable subsidence during the AD 1700 Cascadia earthquake using a Bayesian foraminiferal transfer function. *Bulletin of the Seismological Society of America*, *108*(2), 654–673.
- Kositsky, A. P., & Avouac, J. P. (2010). Inverting geodetic time series with a principal component analysis-based inversion method. *Journal of Geophysical Research: Solid Earth*, *115*(B3), 1–19.
- Loveless, J. P., & Meade, B. J. (2011). Spatial correlation of interseismic coupling and coseismic rupture extent of the 2011 M-W = 9.0 Tohoku-oki earthquake. *Geophysical Research Letters*, *38*, 1–5.
- McCaffrey, R., Long, M. D., Goldfinger, C., Zwick, P. C., Nabelek, J. L., Johnson, C. K., et al. (2000). Rotation and plate locking at the southern Cascadia subduction zone. *Geophysical Research Letters*, *27*(19), 3117–3120.
- McCaffrey, R., Qamar, A. I., King, R. W., Wells, R., Khazaradze, G., Williams, C. A., et al. (2007). Fault locking, block rotation and crustal deformation in the Pacific Northwest. *Geophysical Journal International*, *169*(3), 1315–1340.
- McCrory, P. A., Blair, J. L., Waldhauser, F., & Oppenheimer, D. H. (2012). Juan de Fuca slab geometry and its relation to Wadati-Benioff zone seismicity. *Journal of Geophysical Research: Solid Earth*, *117*(B9), 1–23.
- McGary, R. S., Rondenay, S., Evans, R. L., Abers, G. A., & Wannamaker, P. E. (2011). A joint geophysical investigation of the Cascadia subduction system in central Washington using dense arrays of passive seismic and magnetotelluric station data. In *AGU Fall Meeting Abstracts*.
- Miller, M. M., Melbourne, T., Johnson, D. J., & Sumner, W. Q. (2002). Periodic slow earthquakes from the Cascadia subduction zone. *Science*, *295*(5564), 2423.
- Moreno, M., Rosenau, M., & Oncken, O. (2010). 2010 Maule earthquake slip correlates with pre-seismic locking of Andean subduction zone. *Nature*, *467*(7312), 198–U184.
- Nabelek, J., Trehu, A., Li, X. Q., & Fabritius, A. (1996). *Lithospheric structure of the Cascadia Arc beneath Oregon*. New York: Transactions of the American Geophysical Union.
- Nicholson, T., Bostock, M., & Cassidy, J. F. (2005). New constraints on subduction zone structure in northern Cascadia. *Geophysical Journal International*, *161*(3), 849–859.
- Okada, Y. (1992). Internal deformation due to shear and tensile faults in a half-space. *Bulletin of the Seismological Society of America*, *82*(2), 1018–1040.
- Oleskevich, D. A., Hyndman, R. D., & Wang, K. (1999). The updip and downdip limits to great subduction earthquakes: thermal and structural models of Cascadia, south Alaska, SW Japan, and Chile. *Journal of Geophysical Research-Solid Earth*, *104*(B7), 14965–14991.
- Peltier, W. R., Argus, D. F., & Drummond, R. (2015). Space geodesy constrains ice age terminal deglaciation: the global ICE-6G_C (VM5a) model. *Journal of Geophysical Research: Solid Earth*, *120*(1), 450–487.
- Radiguet, M., Cotton, F., Vergnolle, M., Campillo, M., Valette, B., Kostoglodov, V., et al. (2011). Spatial and temporal evolution of a long term slow slip event: the 2006 Guerrero Slow Slip Event. *Geophysical Journal International*, *184*(2), 816–828.
- Rogers, G., & Dragert, H. (2003). Episodic tremor and slip on the Cascadia subduction zone: the chatter of silent slip. *Science*, *300*(5627), 1942–1943.
- Rondenay, S., Bostock, M. G., & Shragge, J. (2001). Multiparameter two-dimensional inversion of scattered teleseismic body waves 3. Application to the Cascadia 1993 data set. *Journal of Geophysical Research: Solid Earth*, *106*, 30795–30807.
- Satake, K., Wang, K., & Atwater, B. F. (2003). Fault slip and seismic moment of the 1700 Cascadia earthquake inferred from Japanese tsunami descriptions. *Journal of Geophysical Research: Solid Earth*, *108*(B11), 1–17.
- Schmalzle, G. M., McCaffrey, R., & Creager, K. C. (2014). Central Cascadia subduction zone creep. *Geochemistry, Geophysics, Geosystems*, *15*(4), 1515–1532.
- Schmidt, D. A., & Gao, H. (2010). Source parameters and time-dependent slip distributions of slow slip events on the Cascadia subduction zone from 1998 to 2008. *Journal of Geophysical Research: Solid Earth*, *115*(B4), 1–13.
- Scholz, C. H. (1998). Earthquakes and friction laws. *Nature*, *391*(6662), 37.
- Segall, P., & Bradley, A. M. (2012). Slow-slip evolves into megathrust earthquakes in 2D numerical simulations. *Geophysical Research Letters*, *39*(18), 1–5.
- Tapley, B. D., Bettadpur, S., Ries, J. C., Thompson, P. F., & Watkins, M. M. (2004). GRACE measurements of mass variability in the Earth system. *Science*, *305*(5683), 503–505.
- Wada, I., Wang, K., He, J., & Hyndman, R. D. (2008). Weakening of the subduction interface and its effects on surface heat flow, slab dehydration, and mantle wedge serpentinization. *Journal of Geophysical Research: Solid Earth*, *113*(B4), 1–15.
- Wang, P. L., Engelhart, S. E., Wang, K., Hawkes, A. D., Horton, B. P., Nelson, A. R., et al. (2013). Heterogeneous rupture in the great Cascadia earthquake of 1700 inferred from coastal subsidence estimates. *Journal of Geophysical Research: Solid Earth*, *118*(5), 2460–2473.
- Wang, K., He, J., Dragert, H., & James, T. S. (2001). Three-dimensional viscoelastic interseismic deformation model for the Cascadia subduction zone. *Earth, Planets and Space*, *53*(4), 295–306.
- Wang, K., & Tréhu, A. M. (2016). Invited review paper: some outstanding issues in the study of great megathrust earthquakes—The Cascadia example. *Journal of Geodynamics*, *98*, 1–18.
- Wang, K., Wells, R., Mazzotti, S., Hyndman, R. D., & Sagiya, T. (2003). A revised dislocation model of interseismic deformation of the Cascadia subduction zone. *Journal of Geophysical Research: Solid Earth*, *108*(B1), 1–13.
- Wech, A. G., & Bartlow, N. M. (2014). Slip rate and tremor genesis in Cascadia. *Geophysical Research Letters*, *41*(2), 392–398.
- Wech, A. G., & Creager, K. C. (2007). Cascadia tremor polarization evidence for plate interface slip. *Geophysical Research Letters*, *34*(22), 1–6.
- Xu, X., Dong, D., Fang, M., Zhou, Y., Wei, N., & Zhou, F. (2017). Contributions of thermoelastic deformation to seasonal variations in GPS station position. *GPS Solutions*, *21*(3), 1265–1274.